

POLITECNICO DI TORINO

Master's Degree in Biomedical Engineering



Master's Degree Thesis

Nanoparticles For Combinatorial Treatment Of Pancreatic Cancer

Supervisor

Prof. Clara MATTU

Co-supervisors

Prof. Valentina Alice CAUDA

Prof. Gianluca CIARDELLI

Candidate

Erika MONITTOLA

a.a 2020-2021

Summary

Pancreatic ductal adenocarcinoma (PDAC) is the fourth leading cause of cancer death in Europe and in the US. Its detection is difficult because of the lack of clinical signs and disease-specific biomarkers. As a result, most patients remain asymptomatic and the disease results incurable when it is diagnosed. The PDAC microenvironment is characterized by a thick desmoplastic stroma and disorganized blood vessels that impedes an efficient drug delivery, the accumulation of the drug in the specific site and makes this tumour extremely hard-to-treat with traditional chemotherapy. The progression from normal cells to invasive PDAC requires the accumulation of multiple inherited or acquired mutations. Several signalling pathways, such as RAS, PI3K, and Hedgehog (Hh) are known to play a role in supporting tumorigenesis and tumour progression. Treatment options for PDAC are limited and depend on the disease's stage. The tumour can be classified in four main categories depending on tumour extension: resectable, borderline resectable, locally advanced and metastatic. The main treatment for pancreatic cancer is the surgical procedure, however it is restricted to earlier disease stages. Chemotherapy, radiotherapy, and new techniques based on the combination of hyperthermia with nanoparticles remain the main treatments for metastatic tumour. Nanomedicine has great potential in PDAC because of the ability of nanoconstructs to overcome biological barriers and to release the drug in the specific site. A lot of organic and inorganic nanomaterials have been successfully explored as smart functional materials in nanomedicine. Zinc oxide (ZnO) nanoparticles show some interesting properties, such as semiconductive, piezoelectric and antimicrobial behaviours, as well as ease of synthesis in reduced size nanoparticles, that make them easily addressing in the human body and facilitate the cellular uptake. However, the use of ZnO nanomaterials in nanomedicine is still limited because of the intrinsic limitations such as low stability of the ZnO particles in biological fluids and the non-controllable release of Zn^{2+} cytotoxic species. For this purpose, the doping of ZnO served as a powerful approach to confer to ZnO new functionalities. We decided to synthesize ZnO nanoparticles and ZnO nanoparticles doped with Gadolinium which induces a magnetic behaviour in the nanoparticles, useful for further use as contrast agent in magnetic resonance imaging. Polymeric materials result a powerful tool

thanks to their biological stability, reduced renal clearance and ability to co-host multiple drugs. So, many researchers have developed new systems that combine the properties of inorganic nanoparticles with the properties of the polymeric coating. In my Master Thesis work, I have coated the ZnO and the Gd-doped ZnO nanoparticles with a polymer (a proprietary polyurethane) and I have stabilized the system with a lipid bilayer made of L- α -phosphatidylglycerol (EGG-PG) and 1,2-distearoyl-sn-glycero-3-phosphoethanolamine-N-[amino(polyethyleneglycol)-2000] (DSPE-PEG) . The aim was to characterize these nanoparticles and to evaluate their cytotoxicity against pancreatic cancer cells in vitro. Drug-encapsulated nanoparticles (containing Gemcitabine) were also prepared and characterized, in terms of therapeutic effect on pancreatic cancer cells.

Table of Contents

List of Tables	VII
List of Figures	VIII
1 Introduction	1
1.1 The PDAC Microenvironment	1
1.2 PDAC Genetic Progression	3
1.3 PDAC Treatments: state-of-art	5
1.3.1 Traditional Treatments	5
1.3.2 Targeted Therapies	6
1.3.3 Immunotherapy	7
1.3.4 Nanomedicines	8
1.3.5 Nanomedicines in PDAC treatment	8
1.3.6 Zinc oxide (ZnO) nanoparticles	12
1.3.7 Polymeric and Hybrid Nanoparticles	13
1.4 Aim of the work	14
2 Materials and Methods	16
2.1 Coprecipitation method to synthetize undoped and doped Oleate-stabilized ZnO nanoparticles (Ol-ZnO and Ol-ZnO-Gd)	16
2.2 Functionalization method	18
2.3 Characterization Methods	19
2.3.1 Dynamic Light Scattering (DLS) and Zeta Potential	19
2.3.2 X-Ray Diffraction (XRD)	21
2.3.3 Field Emission Scanning Electron Microscopy (FESEM)	24
2.4 Nanoprecipitation method to coat the ZnO nanoparticles	25
2.5 Characterization Methods	26
2.5.1 Freeze-Drying	26
2.5.2 Transmission Electron Microscopy (TEM)	28
2.5.3 Quantification of ZnO loading	29
2.5.4 Viability Assay	29

2.5.5	Fluorescence Activated Cell Sorter (FACS)	30
2.6	Drug encapsulation	31
2.6.1	Viability Assay - Drug-encapsulated Nanoparticles	31
3	Results and Discussion	32
3.1	Uncoated Nanoparticles	32
3.1.1	Dynamic Light Scattering (DLS) and Zeta Potential	32
3.1.2	X-Ray Diffraction (XRD)	37
3.1.3	Field Emission Scanning Electron Microscopy (FESEM)	40
3.2	Coated Nanoparticles	40
3.2.1	Dynamic Light Scattering (DLS) and Zeta Potential	40
3.2.2	Percentage Yield	45
3.2.3	Transmission Electron Microscopy (TEM)	45
3.2.4	Loading of ZnO	46
3.2.5	Viability Assay	47
3.2.6	Fluorescence Activated Cell Sorter (FACS)	51
4	Conclusions	52
	Bibliography	54

List of Tables

3.1	Concentrations of synthesized nanoparticles	32
3.2	Hydrodynamic sizes and polydispersity indexes (PDI) in water. . .	33
3.3	Hydrodynamic sizes and polydispersity indexes (PDI) in ethanol. .	33
3.4	Peaks Classification	38
3.5	Deybe-Sherrer diameters (nm) calculated from FWHM of the peaks with $k = 0,89$ and $\lambda = 1,54059 \text{ \AA}$ - ZnO nanoparticles.	38
3.6	Deybe-Sherrer diameters (nm) calculated from FWHM of the peaks with $k = 0,89$ and $\lambda = 1,54059 \text{ \AA}$ - ZnO-Gd nanoparticles.	39
3.7	Deybe-Sherrer diameters (nm) calculated from FWHM of the peaks with $k = 0,89$ and $\lambda = 1,54059 \text{ \AA}$ - ZnO-funct nanoparticles.	39
3.8	Deybe-Sherrer diameters (nm) calculated from FWHM of the peaks with $k = 0,89$ and $\lambda = 1,54059 \text{ \AA}$ - ZnO-Gd-funct nanoparticles. . .	39
3.9	Hydrodynamic sizes and polydispersity indexes (PDI) in water for coated nanoparticles	41
3.10	FACS average values	51

List of Figures

1.1	PDAC microenvironment [4]	2
1.2	Progression from normal ducts (A) to PanIN-1 (B), PanIN-2 (C) and PanIN-3 (D) [7]	3
1.3	ZnO nanoparticles coated with the polymer and stabilized by lipid bilayer	15
2.1	Coprecipitation method to synthesize nanoparticles	17
2.2	Functionalization method	18
2.3	Zetasizer Nano ZS90	21
2.4	Classic diffractometer setup in Bregg-Brentano geometry with components for reflection measurement [40]	22
2.5	Panalytical X'Pert diffractometer	23
2.6	FESEM schematic components	24
2.7	FESEM instrumentation	25
2.8	Nanoprecipitation method to coat the nanoparticle	26
2.9	Freeze-drying process [44]	27
2.10	ScanVac CoolSafe Freeze Dryer	27
2.11	Components of TEM [46]	28
2.12	Schematic representation of viability assay	29
2.13	Guava® easyCyte™ Flow Cytometer	30
2.14	NPs preparation for FACS analysis	30
3.1	Hydrodynamic sizes and polydispersity indexes (PDI) in (A) water and (B) in ethanol	33
3.2	DLS measurement in intensity % of (A) ZnO, (B) ZnO-Gd, (C) amine-functionalized ZnO and (D) ZnO-Gd nanoparticles in water	34
3.3	DLS measurement in intensity % of (A) ZnO, (B) ZnO-Gd, (C) amine-functionalized ZnO and (D) ZnO-Gd nanoparticles in ethanol	35
3.4	Zeta Potential of all inorganic NPs	36
3.5	X-ray diffractometer of (A) ZnO, (B) ZnO-Gd nanoparticles and amine-functionalized (C) ZnO and (D) ZnO-Gd nanoparticles	37

3.6	FESEM images of (A) undoped, (B) doped, (C) amine-functionalized undoped and (D) amine-functionalized doped nanoparticles	40
3.7	DLS Intensity profiles of PU NPs loaded with ZnO NPs at (A) 20 μg , (B) 50 μg and (C) 100 μg , PU NPs loaded with ZnO-Gd NPs at (D) 20 μg , (E) 50 μg and (F) 100 μg ; PU NPs loaded with amine-functionalized ZnO NPs at (G) 20 μg , (H) 50 μg and (I) 100 μg ; and PU NPs loaded with amine-functionalized ZnO-Gd NPs at (J) 20 μg , (K) 50 μg and (L) 100 μg	42
3.8	Size and PDI for coated (A) ZnO NPs, (B) ZnO-Gd NPs, (C) ZnO-funct NPs, and (D) ZnO-Gd-funct	43
3.9	Zeta Potential for coated (A) ZnO NPs, (B) ZnO-Gd NPs, (C) ZnO-funct NPs, and (D) ZnO-Gd-funct	44
3.10	Average Percentage Yield	45
3.11	(A) TEM image of ZnO control sample; and TEM images of coated NPs loaded with (B) 20 μg , (C) 50 μg and (D) 100 μg of ZnO	46
3.12	Effective loading trend in coated NPs as compared to the starting loading	47
3.13	Control cells BxPC-3 before treatment	47
3.14	Viability assay at (A) 24h and (B) 48h for ZnO and ZnO-PU NPs; and Viability assay at (C) 24h and (D) 48h for ZnO-Gd and ZnO-Gd PU NPs	48
3.15	Cells treated with (a) 5 $\mu\text{g}/\text{mL}$, (b) 10 $\mu\text{g}/\text{mL}$, (c) 25 $\mu\text{g}/\text{mL}$ and (d) 50 $\mu\text{g}/\text{mL}$ of ZnO NPs after 24 hours	49
3.16	Cells treated with (a) 5 $\mu\text{g}/\text{mL}$, (b) 10 $\mu\text{g}/\text{mL}$, (c) 25 $\mu\text{g}/\text{mL}$ and (d) 50 $\mu\text{g}/\text{mL}$ of ZnO NPs after 48 hours	49
3.17	Cells treated with (a) 5 $\mu\text{g}/\text{mL}$, (b) 10 $\mu\text{g}/\text{mL}$, (c) 25 $\mu\text{g}/\text{mL}$ and (d) 50 $\mu\text{g}/\text{mL}$ of ZnO-PU NPs after 24 hours	50
3.18	Cells treated with (a) 5 $\mu\text{g}/\text{mL}$, (b) 10 $\mu\text{g}/\text{mL}$, (c) 25 $\mu\text{g}/\text{mL}$ and (d) 50 $\mu\text{g}/\text{mL}$ of ZnO-PU NPs after 48 hours	50
3.19	FACS analysis outcomes for (A) untreated cells (control) and cells treated with (B) ZnO NPs and (C) ZnO-PU NPs	51

Chapter 1

Introduction

1.1 The PDAC Microenvironment

Pancreatic ductal adenocarcinoma (PDAC) is the fourth leading cause of cancer death in Europe and in the US. The overall survival at 5-year post-diagnosis is <10 % [1]. The main problem is that most patients remain asymptomatic for a long time, and the absence of symptoms and of disease-specific biomarkers makes early diagnosis hard [1]. The tumour microenvironment (Fig. 1.1) hampers efficient drug delivery and the accumulation of the drug at the target site. PDAC is composed of a reduced part of malignant cells (<20 % of the tumour mass) within a microenvironment of fibroblasts, endothelial cells, and immune cells (70 %) embedded in a dense extracellular matrix (ECM) composed of fibrin, collagen, hyaluronan, and fibronectin [1]. In normal conditions, the pancreatic stellate cells (PSCs), which are the resident cells of the pancreas, are quiescent and regulate extracellular matrix production [2]. In tumors they become activated and secrete abundant ECM proteins [3]. During tumour progression, PSCs differentiate into two subtypes of cancer-associated fibroblasts, with a pro-inflammatory or a pro-fibrogenic phenotype [1]. The heterogeneity of these activated fibroblasts explains the difficulty to target these cells with specific treatments. [5]. Fibroblasts secrete several factors that negatively affect the tumour microenvironment, such as cytokines and growth factors that actively recruit monocytes and CD4 regulatory T cells (Treg) that contribute to immunosuppression [3]. Most immune infiltrates are cells of the myeloid lineage, with both granulocytic and monocytic myeloid-derived suppressor cells (MDSCs), as well as tumour-associated macrophages (TAMs) contributing to local immunosuppression [3]. Macrophages and MDSCs in tumours have some suppressive functions, such as the capture of metabolites thanks to the presence of the cysteine transporter Slc7A11, the generation of arginase and of indoleamine 2,3-dioxygenase, the maintenance of intra-tumoral

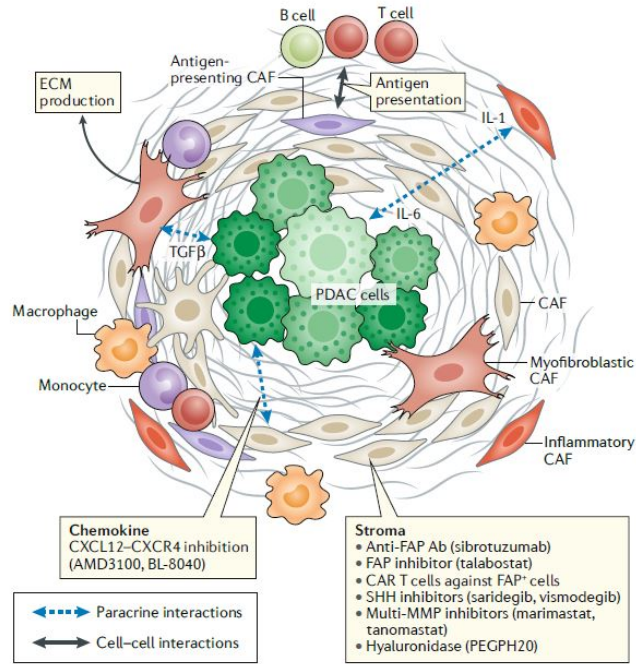


Figure 1.1: PDAC microenvironment [4]

Treg, the inactivation of CD8 T cell proliferation, and the generation of nitric and reactive oxygen species that can alter proteins [3]. Pancreatic tumour cells produce Granulocyte-macrophage colony-stimulating factor (GM-CSF) that causes the accumulation of MDSCs and limits T cells responses. The presence of T cells in pancreatic tumours is controversial. Some researchers have found both CD4 and CD8 T-cell infiltrates [3] in about a quarter of human tumours. This could be explained by the fact that T cells are in tertiary lymphoid structures or aggregates of T and B cells are on the periphery or isolated from the tumour [3]. The PDAC microenvironment is characterized by a lack of blood vessels leading to a state of hypoxia in the tumour. The uninterrupted generation of a dense stroma lead to a generation of solid stress and to the breakdown of the lymphatic drainage in the centre of the tumour. This concurs to increase the intratumoral interstitial fluid pressure (IFP) and generates vessel compression, reduced perfusion, and an hypoxic environment [1]. As a result, most blood vessels in PDAC are non-functional, slightly fenestrated, and surrounded by a dense layer of pericytes that hampers an effective accumulation of drugs or nanomaterials into the tumour [1].

1.2 PDAC Genetic Progression

The progression from healthy cells to invasive PDAC needs the presence of different inherited or acquired mutations [6]. Point mutations in KRAS oncogene are present approximately in the 90 % of all PDACs and represent a premature event of the development of the PDAC [6]. The inhibition of several tumour suppressor genes, such as those coding for p16INK4A, p53, and SMAD4, also concurs to the transformation of the precursor lesion into an infiltrating cancer. PDAC arises from early precursor lesions with increasing histological grades, which are termed pancreatic intraepithelial neoplasia (PanIN), followed by progression to invasive adenocarcinoma [4]. PanINs are classified in three categories [6] (Fig. 1.2).

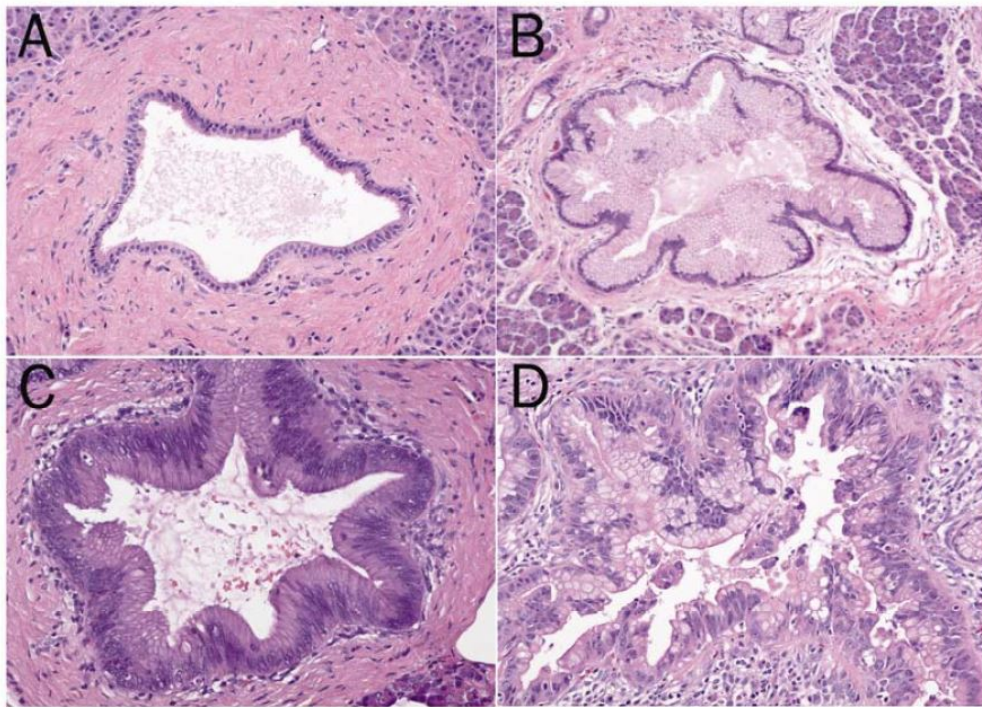


Figure 1.2: Progression from normal ducts (A) to PanIN-1 (B), PanIN-2 (C) and PanIN-3 (D) [7]

- Low-grade (PanIN-1A or 1B): PanIN-1 lesions are made of columnar epithelial cells with round nuclei uniformly distributed and basally oriented [7]. They present a flat (PanIN-1A) or papillary (PanIN-1B) mucinous epithelium without any signs of cellular atypia [8].
- Intermediate (PanIN-2): PanIN-2 have more variations in nuclear disposition, including loss of nuclear polarity, nuclear crowding, change in nuclear size

(pleomorphism) and hyperchromasia, [7]. They show cellular atypia and a predominantly papillary architecture [8].

- High-grade (PanIN-3): PanIN-3 corresponds to carcinoma in situ [8] with the greatest degree of dysplasia [7].

There are also two other non-invasive lesions that could anticipate PDAC formation: intraductal papillary mucinous neoplasms (IPMNs) and mucinous cystic neoplasms (MCNs). These lesions present different mutations in comparison with PanINs. Like PanINs, IPMNs and MCNs can contain the same KRAS pathway and inactivating mutations. Moreover, these two neoplasms can also have distinct mutations. In some instances, MCNs may leak SMAD4 activity while IPMNs usually do not [6]. The activating point mutation in KRAS gene generally happens at codon 12 and concerns a replacement of glycine with aspartic acid, valine, arginine, or serine [6]. This mutation causes a decrease of the intrinsic GTPase activity of KRAS (GTPase protein is involved in the signal transduction across the cellular membrane. The KRAS gene can bind this protein and can become activated) and makes the activated protein not sensitive to GTPase-activating proteins [6]. Because of the mutations, several pathways are stimulated, including the RAF-mitogen-activated protein kinase pathway (MAPK) and the phosphoinositide 3-kinase pathway that manage, among others, proliferation, cell division and gene expression. The mutation in KRAS gene is also responsible for the proliferation of the desmoplastic stroma and for the ineffectiveness of some chemotherapeutic treatments. Another consequence of mutant KRAS is the activation of Hedgehog signalling which affects stroma through paracrine signalling [6]. The mutant KRAS is not the only genetic alteration observed in PDAC. In PDAC, telomere length is more reduced compared to normal condition [6]. This causes telomere dysfunction and chromosomal abnormalities. Telomere shortening is visible in the first phases of PDAC progression, it precedes the KRAS mutations, and is in low-grade PanINs, IPMNs [6]. Another event that precedes cancer formation is the inactivation of tumour suppressor genes, the most common of which is CDKN2A (in low-grade or intermediate PanINs), which encodes for the p16INK4A protein that is an inhibitor of the cyclin D-dependent kinases CDK4 and CDK6 and interrupts the cell cycle before the access in the S-phase. Others inactivated genes are TP53 (late event) that encodes for the p53 protein that manages the G1-S cycle checkpoint, arrests the G2-M, and causes apoptosis; and SMAD4 (late event) which encodes for SMAD4 protein that acts as transducer of growth factor β . Despite the advances in understanding the genetic progression of PDAC, the detection of this cancer remains difficult, highlighting the need to develop new improved therapeutic and diagnostic means to detect early stage PDAC [6].

1.3 PDAC Treatments: state-of-art

1.3.1 Traditional Treatments

Treatment options for PDAC are confined and depend on the tumour stage [5]. Computed tomography (CT) combined with a 3D reconstruction, endoscopic ultrasound, magnetic resonance imaging, or laparoscopy are the imaging techniques employed to properly categorize the tumour. PDAC is classified into four major classes based on tumour extension: resectable, borderline resectable, which shows venous involvement of superior mesenteric vein/portal vein and gastroduodenal artery encasement, locally advanced and metastatic [5]. The first line treatment for pancreatic cancer at earlier stages is the surgical procedure [5]. Chemotherapy, radiotherapy, and new techniques based on the combination of the hyperthermia with ferromagnetic nanoparticles are the primary treatment options for metastatic PDAC [5]. Common side effects of these treatments include decrease in blood cell counts, vomiting, nausea, diarrhea, poor appetite, hair loss, nervous system changes, and infertility [5]. These effects are mainly due to the intrinsic toxicity and to the non-specificity of the treatment. The first drug used in PDAC treatment is the fluoropyrimidine 5-fluoroacil (5-FU), a water-soluble drug with poor and short biological half-life due to its fast metabolism. It can also cause undesired adverse effects such as dermatological reactions, and cardiac and gastrointestinal side effects [9]. Gemcitabine (GEM) is an alternative drug treatment, which was approved by the FDA in 1998. This drug presents better outcome over 5-FU: a comparative study reported a clinical benefit response of 23.8 % in patients treated with GEM with respect to 4.8 % of patients treated with 5-FU [5]. The median survival time was 5.6 and 4.4 months, and the one-year survival rate was 18% and 22% for GEM and 5-FU-treated patients, respectively. [5]. The use of GEM also causes some side effects such as haematological toxicity, fever, and vomiting. Other drugs used in PDAC treatment are:

- Marimastat: an inhibitor of matrix metalloproteinases (MMPs) which are proteolytic enzymes expressed in PDACr. The imbalance of MMPs and tissue specific inhibitors is the basis of the ECM degradation and the tumour invasion. Therefore, inhibiting MMPs to limit the growth of the tumour is a promising approach in PDAC treatment.
- Doxorubicin (DOX): has a low oral bioavailability wich depends on its low intestinal absorption that limits its efficacy in treating cancer.
- Paclitaxel (PTX): is a water insoluble anticancer drug. The conjugation of GEM with albumin-bound Paclitaxel (Abraxane) has been used for advanced pancreatic cancer [5]. This drug combination has shown promising results, by virtue of the facilitated delivery due to the presence of albumin. However,

there were also adverse effects such as neutropenia, leukopenia, neuropathy, febrile neutropenia, or fatigue. The FDA approved the Abraxane-GEM as the first-line therapy option in case of severe and metastatic pancreatic cancer despite of its side effects.

- Docetaxel: is more soluble in water than PTX and is stable in tumor cells for a long time. Its side effects concern hypersensitivity reactions, fluid retention and neutropenia.

Recently, FOLFIRINOX (irinotecan, oxaliplatin, fluorouracil, and leucovorin), a multidrug combination, has been tested to treat metastatic PDAC [5]. Patients treated with FOLFIRINOX showed a higher efficacy with regard to overall survival (11.1 vs 6.8 months), progression-free survival (6.4 vs 3.3 months) and one-year survival rate (48.4 % vs 20.6 %), when compared to GEM alone [5]. Unfortunately, the study showed an increase of side effects, including thrombocytopenia, febrile neutropenia, diarrhea, and a general reduction of quality of life using FOLFIRINOX.

1.3.2 Targeted Therapies

Considering the heterogeneous microenvironment of PDAC and the complex stromal interactions, targeted strategies rarely obtained clinical improvements with respect to the standard treatments. One of the few successful strategies included erlotinib, an epidermal growth factor receptor (EGFR) inhibitor, coupled with GEM. EGFR is part of ErbB family of receptors, with a tyrosine kinase domain, and it manages some important processes such as cell cycle, cell survival and differentiation, activating different downstream signalling pathways, including MAPK/ERK [5]. Molecules that target this pathway have been tested: for example, antibodies that block EGFR activation and inhibitors of the tyrosine kinase domain of the receptor [5]. Another possibility is to develop target therapies against the human epidermal growth factor receptor 2 (HER-2), since HER-2 over-expression is correlated with scarce patient survival. Insulin-like growth factor 1 receptor (IGF1R) is also over expressed in PDAC, and this causes an extreme stimulation of downstream pathways with a consequent increase of cell proliferation and survival. Membrane-bound guanosine triphosphate hydrolase (GTP-ase) protein, encoded by KRAS gene, is activated by the EGF. [5]. In case of mutations, some signalling pathways (such as MAPK/ERK, PI3K/Akt) are activated, increasing signals of proliferation and inhibition signals of cell apoptosis. Therefore, strategies targeting proteins along the KRAS signal transduction pathway have been developed [5]. To reach this purpose, rigosertib (a small molecule inhibitor of PI3K) in combination with gemcitabine, or tipifarnib (an inhibitor of farnesyltransferase that is an essential effector of RAS) in combination with GEM have been tested. The vascular endothelial growth factor (VEGF) and its receptor are other possible targets: therapy against these molecules

could decrease proliferation of endothelial cells and infiltration and metastasis in vivo. However, the anti-angiogenic agents with VEGF inhibitors, such as Axitinib and Avastin, did not show positive results. Combining Gemcitabine with VEGF inhibitor resulted in promising preclinical results, which were unfortunately not replicated in patients. Since cancer-associated stromal cells are known to influence PDAC progression, some studies proposed the use of nab-paclitaxel/gemcitabine to combine the anti-cancer effect of GEM with the cytotoxicity against cancer-associated fibroblasts and stroma disruption of nab-paclitaxel [5]. The Hedgehog pathway (SHH) controls the generation of the desmoplastic stroma. The inhibition of the Hedgehog pathway by pharmaceutical inhibitors agents (IPI-926) has a potential anti-tumour activity. The combination of IPI-926 and Gemcitabine (or nab-paclitaxel) has shown improved drug delivery, reduced metastases, and higher survival rate. Currently, no FDA-approved Hedgehog inhibitors are available, but clinical trials are under evaluation [5]. Vismodegib (GDC-0049), another inhibitor of the Hedgehog pathway, is also under assessment in combination with Gemcitabine and with Gemcitabine/nab-Paclitaxel for metastatic patients [5]. Another molecule identified as possible target is Tissue Growth Factor (TGF) which is over expressed in PDAC tissues. Similarly, target therapies against Pancreatic stellate cells (PSCs) and other ECM proteins have been proposed, since PSCs actively are involved in the production of the stroma. Angiotensin II type 1 receptor blockers (ARBs) had the best results [5]. Among these, Candesartan, could suppress PSCs activation and prolonged the survival for more than 6 months when coupled with ACEIs (angiotensin I converting enzyme inhibitors) [5]. Losartan, another ARBs, was shown to decrease the quantity of hyaluronan and collagen in the tumour stroma, remodel tumour micro environment and increase blood perfusion [5].

1.3.3 Immunotherapy

Immunotherapy is an emerging treatment for advanced PDAC. This approach exploits immune checkpoint inhibitors, such as programmed death receptor (PD-1) and its ligand PD-L1, which are expressed on tumour-associated lymphocytes and participate in the inhibition of immune response during carcinogenesis. Targeting this signalling pathway should activate T cell activity and therefore cancer cell death [5]. Another strategy is to target CD40 which is a tumour necrosis factor expressed by immune cells. Its over expression is linked with cancer progression. Enhancing CD40 activity with its agonists may increase T-cell immune responses and consequently induce cancer regression [5]. The use of CD40 agonist in combination with GEM could enhance the store of tumour-suppressive macrophages and reduce the tumour progression. Other applications of the immunotherapy concern the vaccines, that improve the response of the immune system to the tumour-associated antigens [5], monoclonal antibodies, which exploit T cell therapy

that is based on the pickup of patient's T cells, then their activity is boosted through genetic/chemical re-engineering, and at the end they are reintroduced into the patient, and use of cytokines. [5]. Virus therapies are currently under assessment as anti-cancer tools because they can facilitate the auto disruption of the cells.

1.3.4 Nanomedicines

Nanomedicine uses nanoparticles (1-100 nm) combined with drugs and pharmaceutical ingredients, overcoming the specificity and toxicity problems of the traditional treatments [10]. Many nanomaterials, both organic and inorganic, have been successfully used in the design of nanomedicines. Nanoparticles offer several advantages in drug delivery, as detailed below:

1. They allow high encapsulation efficiency of drugs and their controlled release at the site of interest, improving pharmacokinetics and biodistribution of the encapsulated drug [11].
2. By doing so, they overcome some of the main restrictions of conventional treatments based on chemotherapy, such as the lack of selectivity and solubility and the side effects.
3. Nanoparticles have high surface area and can be surface modified with targeting ligands to achieve higher tumor selectivity. Moreover the reduced size (5–100 nm) allows their passive accumulation in tumours through the Enhanced permeability and Retention (EPR) effect. [11].
4. They offer stimuli-triggered release options, such as pH-triggered release or release activated by external light/mechanical stimulation (smart nanoparticles).
5. Nanoparticles can also be employed as contrast agents with enhanced imaging properties. For instance, magnetic nanoparticles have been used as contrast agents in MRI [11], while metallic nanoparticles have successfully been used as contrast agents for optical and X-ray imaging.
6. Imaging and treatment options can be combined in an all-in-one system (theranostic nanoparticles) to achieve detection/follow-up ability coupled with site-specific drug release.

1.3.5 Nanomedicine in PDAC treatment

The most common class of nanomedicines used for PDAC treatment are nanocarriers loaded with synthetic drugs. Considering the good effects obtained with GEM

treatments, nano-sized drug delivery systems carrying GEM have been produced to enhance target accumulation and reduce systemic toxicity [9]. For example, GEM-modified gold nanoparticles have been synthesized using cetuximab (anti-EGFR antibody – EGFR is the epidermal growth factor receptor which is overexpressed in PDAC and is involved in carcinogenesis) as a targeting agent. The system was tested *in vitro* on three pancreatic cancer cell lines (PANC-1, AsPC-1, and MIA-Paca2) [12] and the results demonstrated that the targeted nanoparticles presented a higher inhibition ability of PDAC cells proliferation when compared to the non-targeted ones [9]. Another study has combined GEM with iron oxide magnetic nanoparticles (MNPs) and anti-CD47 antibody to reduce the growth of the tumour [9]. The system was tested both *in vitro* on Panc-215 and Panc-354 cells, and *ex vivo* on human PDAC tissues obtained by patients and expanded as patient-derived xenografts [13]. The study showed a suppressed growth of pancreatic tumours and an improvement in the imaging contrast in magnetic resonance imaging (MRI) [13]. To target the characteristic vascular tissue of PDAC, researchers have combined GEM with PEGylated human recombinant PH20 hyaluronidase (PEGPH20) and tested it in mice. It is known that the deposition in the interstitium of hyaluronan (HA) is partially responsible for the generation of high interstitial pressure in many solid tumours and of the consequent vascular collapse and hypo-perfusion [14]. By using PEGPH20 it is possible to target and degrade hyaluronic acid, thus reducing intra-tumoral pressure and normalizing the vasculature. Tumours treated with this combination showed a decreased size at the end of the treatment, but an increase in the metastatic potential was also observed [14]. Another nanomedicine-based approach was based on large pore-sized GEM-loaded mesoporous silica vesicles (MSVs) [9], which showed higher internalization into PDAC cells compared to free GEM employing both Pan02 and BxPC-3 cells line. This is of particular note since GEM is quickly transformed into its inactive metabolite 2',2'-difluorodeoxyuridine (dFdU) by cytidine deaminase after systemic administration and it is also too hydrophilic to cross the cell membrane [15]. Therefore, the proposed system was able to preserve the encapsulated drug from enzymatic metabolism, and enhanced penetration through the cell, improving Gemcitabine efficiency [15]. The developed MSVs showed large pore size and volume useful for efficient drug loading [15]. Graphene quantum dots (GQD) have also been proposed. GQD-conjugated GEM-loaded human serum albumin (HSA) was tested on Panc-1 cancer cells with good uptake and low toxicity effects [9]. Since early detection and surgical resection raise the mean 5-year survival of PDAC patients up to 31.7 ± 3.6 months, there is ample room to exploit the tumour-accumulation ability of theranostic nanoparticles to transport imaging agents for early detection of PDAC in combination with treatments [1]. For example, magnetic nanoparticles combined with mesoporous silica nanoparticles have been used to maximize the drug loading efficiency (because of their high surface area) and as stimuli-responsive release system [11]. Maghemite

nanoparticles placed in mesoporous-silica matrix allow magnetic hyperthermia under exposure to a low-frequency alternating magnetic field [16]. The possibility to vary the intensity of the generated heat together with the biocompatibility of the system and the good uptake in cancer cells *in vitro* represents a new tool against solid tumors. Recently, researchers have developed new platforms which combine photothermal therapy with a chemotherapeutic agent (photochemotherapy). An example concerns a hybrid NPs loaded with GEM inside a polymer matrix in a nano-gold NPs system [17]. The samples were irradiated with a laser at 640 nm for 10 minutes, recording the temperature every minute. The temperature of the hybrid NPs rose by 12.3°C in 10 minutes while the only gold NPs showed an increase of only 2.5°C [17]. This meant that the hybrid system converted more efficiently the light into thermal energy [17]. This was due to the presence of the polymeric matrix which enhanced the clustering of the nanoparticles [17]. The cytotoxicity was tested on MiaPaca-2 cell line as a function of GEM concentration. The cells treated with only GEM or with gold nanoparticles showed a ratio of apoptosis to necrosis of 70:30 with or without laser irradiation. On the contrary, the cells treated with the hybrid GEM-polymer nanoparticles showed an apoptosis/necrosis ratio ranging from 75:25 to 60:40. [17], indicating that the thermal effect increased the efficacy of GEM. The second group of techniques used for PDAC treatment, is composed by metals and metal oxides nanoparticles with anti-pancreatic cancer activity. Superparamagnetic iron oxide NPs were used to convert the absorbed energy from alternating magnetic fields into heat in a murine B16-F10 melanoma. [18]. After the intratumoral injection and the exposition to short external alternating magnetic field, there was an important reduction in tumor size [18]. Cerium oxide NPs were also tested in pre-clinical trials as an adjuvant to sensitize PDAC cells to radiation therapy (RT), showing a decrease in tumour weight and volume and protecting healthy tissues from the harmful adverse effects [19]. Cerium oxide NPs combined with RT induced the activation of c-Jun terminal kinase (JNK) which induces apoptosis [19]. Furthermore, these nanoparticles stimulated the generation of reactive oxygen species (ROS) in cancer cells which induced the oxidation of thioredoxin 1 (TRX1) and the consequent stimulation of apoptosis signaling kinase 1 (ASK1) [19]. These NPs re-activated the apoptotic mechanism in the human PDAC cells when submitted to RT [19]. Magnetic Fe₃O₄ NPs conjugated with Gambogic Acid (anti-cancer drug with poor water solubility) were tested in Capan-1 pancreatic cancer cells showing enhanced chemotherapeutic efficiency [20], as demonstrated by the reduced expression of antiapoptotic proteins, such as Bcl-2, and the increased expression of proapoptotic ones, including Bax, Caspase 9 and Caspase 3 [20]. Silver-graphene quantum dots were also demonstrated to be specific for pancreatic cancer without affecting normal tissues. Carboxy methyl inulin (CMI) was bound to the nanocomposite to increase its biocompatibility and 5-FU was used to investigate the anticancer effect. [21]. The system was

tested in vitro on Panc-1 cells and in vivo on a PDAC model in Wistar Rats [21]. The presence of CMI effectively reduced the toxicity of the metal NPs [21] as demonstrated by the absence of abnormalities in the normal tissues near the cancer site. Gold NPs with Plectin-1-peptide conjugated with Gemcitabine showed selective accumulation in PDAC tissues as demonstrated by the in vitro test on PDAC cell lines (AsPC-1 and PANC-1) and by the in vivo test in Panc-1 orthotopic xenograft model [22]. It has been demonstrated that these NPs have a good efficiency in accumulating in tumors expressing plectin-1 without affecting adjacent normal pancreatic tissue. Furthermore, they were able to deliver GEM selectively to cancer cells [22]. PEGylated graphene oxide nano-sheets were used as gene delivery system to co-deliver Histone deacetylase (HDAC1) and KRAS siRNAs to target MIAPaca-2 pancreatic cancer cells. [23]. PEG was used to increase the biocompatibility. HDAC1 is involved in maintaining of the pluripotency of embryonic and cancer stem cells. KRAS mutation is typical of PDAC progression as previously described. This study demonstrated also how the combination of this nanosystem with near-infrared (NIR) light inhibited in vivo tumor growth rate by over 80 % in mice [23]. This outcome revealed the importance of the photothermal effects in anticancer treatment.

Another class of nanoparticles are the so-called smart nanosystems, which are planned to react to external stimuli to trigger drug release once they have passively or actively reached the tumour site [1]. For example, smart nanoparticles that respond to temperature or pH stimuli can be designed. Temperatures over 42°C induce cell death in normal tissues, while temperatures over between 41°C and 47°C induce apoptosis and over 50°C induce necrosis in tumor [24]. Therefore, hyperthermia has been associated with other traditional treatments in PDAC. Oluwasanmi et al. [25] developed hybrid nanoparticles (HNP) coupled with GEM through a Diels Alder linker. The heat was produced by a laser and was used to irradiate the HNPs promoting the breakdown of the linker and the release of the drug. The system was evaluated in vitro on pancreatic cancer cells showing an 11-fold improvement in cellular uptake and a higher performance in terms of cytotoxicity as compared to the GEM-loaded nanoparticles without the heat generation [25]. In vivo the nanosystem showed a 62 % reduction in tumour weight and size in pancreatic BxPC-3 xenografts when compared to the same system without irradiation [25]. Ray et al. [26] developed a system composed of 4-amino-4'-dimethylaminoazobenzene (AZB), isoleucine (Ile) copolymers and poly(ethylene)glycol-block-poly (carbonate) (PEG-b-PC) loaded with GEM. The copolymers respond to pH variations. The nanoparticles had a size of 114-137 nm depending on the copolymers used. This PEG-b-PC system was able to encapsulate GEM at 13.8 - 28.8 % and, when the copolymers were activated by a pH change, to release the drug [26]. At the low pH of the cellular compartments, NPs are disassembled [26]. Nanoparticles can also be designed to react to the application of

magnetic fields to produce heat at the target site. For example, gold-silica nano shells have been developed to treat malignant cancer by heating the tumor cells [24].

1.3.6 Zinc oxide (ZnO) nanoparticles

The thesis focuses on the use of zinc oxide nanoparticles in PDAC treatment. Zinc oxide (ZnO) is a low-cost, abundant, and inorganic material [11]. It is a GRAS (“Generally Recognized as Safe”) material at the micrometric level, however it shows a concentration-dependent toxicity at nanometer-size level when in contact with cells, specifically cancer ones. ZnO is also a wide band-gap semiconductor (3.31 eV) with interesting physical and chemical properties, such as photo- and sono-catalytic activities, piezoelectricity, and pyroelectric behaviour [11]. ZnO nanoparticles (NPs) can easily reach specific site in the human body and can accumulate efficiently in tumours thanks to their reduced size [27], which also facilitate cellular uptake. Nanoparticles size and overall shape allows their internalization into cells and their interactions with biomolecules inside or on the cell surface in cancer treatment [28]. ZnO nanoparticles also showed good antimicrobial properties against both Gram-positive and Gram-negative bacteria [11]. The antimicrobial properties derive from a combination of chemical and physical interactions between the microorganism and zinc oxide, represented by electrostatic forces that favour the release and the consequent penetration in the microorganisms of cations and reactive oxygen species [29]. ZnO has the ability to encourage the growth and the proliferation of different cell lines thanks to its antimicrobial propriety, both in non-structures and in 3D structures [30]. Despite these good results, the application of ZnO nanomaterials in nanomedicine is still restricted because of intrinsic limitations such as low stability of the ZnO particles in biological fluids and the uncontrollable release of Zn^{2+} cytotoxic species [11]. Several studies have analyzed the cytotoxicity of ZnO due to the overproduction of reactive oxygen species and to the release of zinc ions [31]. The electrostatic nature of the nanoparticles is involved in cellular adhesion and uptake. The mechanism of cytotoxicity from ZnO nanoparticles is not completely understood, but it seems to be predominantly due to the release of reactive oxygen species (ROS) [28]: when nanoparticles and cells interact, the mechanism of defense of the cells is activated. If the presence of ROS is elevated, an oxidative damage caused to biomolecules in the cells, leading to cell death [28]. Several studies were carried out to evaluate the ZnO cytotoxicity on different types of cancer cells. The total body zinc content is around 2g and it is useful to maintain organ and cells integrity. Alterations in this concentration may cause problems in cellular processes. Some studies report a higher ZnO cytotoxicity on cancer cells versus normal cells (around 28-35 times with respect normal cells) [32]. This could be explained by considering that the blood vessels in tumours present large pores

which allow an easier penetration of the nanoparticles in cancer sites or a higher sensibility of the cancer cells to non-physiological level of intracellular Zinc cations and ROS. Another factor which plays a role in determining the cytotoxic effect of ZnO nanoparticles is their charge: ZnO nanoparticles present a positive charge, while cancerous cells usually have high concentration of anionic phospholipids on their membrane [32]. Thus, there is an electrostatic attraction that encourages selective accumulation of ZnO NPs in the tumour and consequently a cytotoxicity effect. The toxicity was studied *in vitro* on BxPC-3 pancreatic adenocarcinoma cell line. In the literature 10 $\mu\text{g}/\text{mL}$ to 20 $\mu\text{g}/\text{mL}$ is reported as safe concentration range of ZnO nanoparticles for cytotoxicity test [32].

For this reason, the doping of ZnO represents a useful tool to give new functionalities or to enhance pre-existing ones. For example, the optical, electrical, electromechanical, and catalytic properties could be enhanced after doping ZnO with proper elements [11]. Doping represents a new possibility to design a multifunctional theranostic nanoplatform that can perform both diagnosis and therapy at the same time [11]. The ion's dimension, the electronegativity, the coordination state, etc., all contribute to determining the final properties of the doped material [11]. According to Carofiglio et al. [11] the most used dopants are: (1) Gadolinium, which is a Rare Earth element and induces a magnetic behaviour in ZnO nanoparticles as reported in the article of Barui et al. [29]; (2) Iron, which improves chemical stability of the ZnO nanoparticles in aqueous media and enhances the electromechanical response as described in the article of Carofiglio et al. [33]; (3) Manganese, described by Barui et al. [29] which is used to modify the optical, structural, and magnetic properties of the resulting ZnO semiconductor; (4) Copper, which increases the antimicrobial activity of ZnO as demonstrated by Maddahi et al. [31].

1.3.7 Polymeric and Hybrid Nanoparticles

Polymeric nanoparticles present several advantages such as such low toxicity profile, enhanced tumour accumulation through passive and active targeting mechanisms, reduced renal clearance, and possibility to co-host multiple drugs [34]. To combine the properties of inorganic nanoparticles with polymers, researchers have developed new hybrid systems based on inorganic nanoparticles as core materials coated with a polymeric shell. For example, to improve the biodistribution performance of AuNPs and their ablation properties, spherical gold nanoparticles have been encapsulated into a larger polymeric nanoconstructs. The resulting gold-loaded spherical polymeric nanoconstructs were constituted by a polymer matrix in which AuNPs are encapsulated, and by a surface lipid monolayer used to stabilize the system and provide long circulation capability [35]. Dumontel et al. [27] demonstrated how the presence of a phospholipid bilayer (1,2-dioleoylsn- glycerol-3-phosphocholine DOPC) on ZnO nanocrystals improve the colloidal and chemical stability in biological and

simulated media. This results also in a decreased cytotoxicity and in a better cellular internalization of this hybrid nanoconstruct. They tested ZnO nanocrystals, amino-propyl functionalized ZnO-NH₂ nanocrystals and phospholipidic-shielded ZnO-DOPC nanocrystals and concluded that the presence of a self-assembled phospholipid bilayer makes the nanoconstruct more stable and prevents the dissolution into zinc cations. A new approach is based on the use of polymer as coating to increase the biocompatibility and to reduce the toxic effect of inorganic nanoparticles [28].

1.4 Aim of the work

The aim of this work is to develop a composite nanosystem for imaging and treatment of PDAC, by combining the therapeutic and imaging capability of ZnO or ZnO-Gd with the long-circulation and ease of surface modification of polymer nanoparticles. To achieve this, ZnO and ZnO-Gd nanoparticles of small size will be synthesized via a co-precipitation method and characterized in terms of size and surface charge, morphology and crystalline structure. To impart long circulation properties, ZnO and ZnO-Gd NPs will be coated with a hybrid polymer/phospholipid shell by using the nanoprecipitation method. In details, we will use a proprietary polyester urethane as the polymer component and L- α -phosphatidylglycerol (EGG-PG) and 1,2-distearoyl-sn-glycero-3-phosphoethanolamine-N-[amino(polyethyleneglycol)- 2000] (DSPE-PEG-amine) to form the lipid bilayer (Fig. 1.3 - Figure made with Biorender.com). The polymer/lipid coated nanoparticles will be fully characterized in terms of surface charge, size, and morphology to confirm the presence of the core-shell structure, and in terms of yield and loading efficiency of ZnO and ZnO-Gd. Moreover, their concentration-dependent cytotoxicity and cell internalization will be evaluated against BxPC-3 pancreatic cells in vitro to verify whether the polymer/lipid coating can improve biocompatibility and cell affinity of the inorganic core. Finally, we will prepare drug doped ZnO nanoparticles (with GEM) and embed them in the polymer core. The efficacy of the drug treatment will be evaluated at different concentrations on BxPC-3 pancreatic cancer cells.

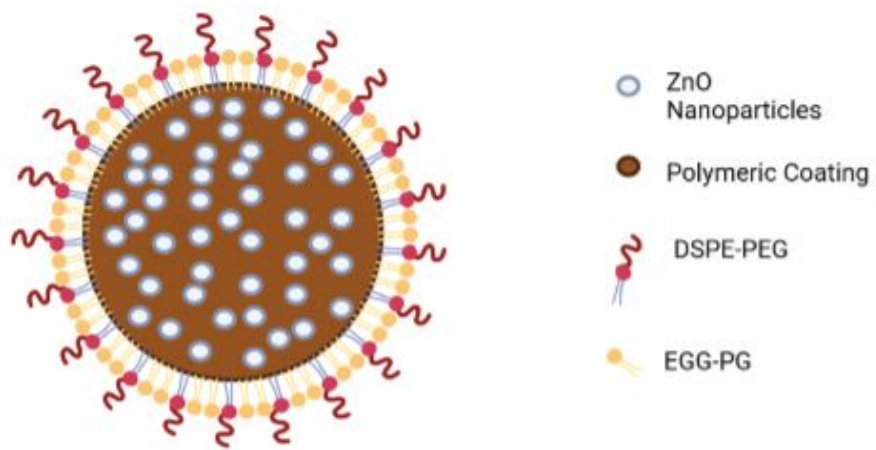


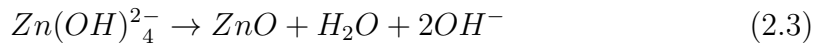
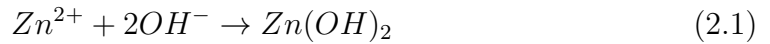
Figure 1.3: ZnO nanoparticles coated with the polymer and stabilized by lipid bilayer

Chapter 2

Materials and Methods

2.1 Coprecipitation method to synthesize undoped and doped Oleate-stabilized ZnO nanoparticles (Ol-ZnO and Ol-ZnO-Gd)

The synthesis of Zinc oxide nanoparticles was conducted via a wet chemical method, in particular a co-precipitation method for both the undoped and Gadolinium doped ZnO NPs, as previously reported by Barui et al. [29]. Wet chemical methods represent a promising tool to obtain nanoparticles with good purity. The reactions of this technique are the following ones [11]:



The process happens in presence of a mineralizing agent which supplies OH^- groups requested to set the pH to avoid the precipitation of zinc hydroxide promoting the formation of ZnO [11]. Generally, the zinc precursor is a zinc acetate, nitrate or chloride because they can dissolve rapidly in most common reaction solvents, such as water or ethanol [11]. The inclusion of dopant can be made mixing the zinc precursor with the dopant ion solution. This co-precipitation method is generally fast when compared to others wet chemical methods, such as the sol-gel synthesis. This means that the time of the process results reduced from hours to several minutes [29]. This method allows to obtain spherical nanoparticles with a small size [29]. The presence of the oleic acid is useful to stabilize the nanoparticles

avoiding their aggregation and to control their size and shape [29]. The whole process is reported in Figure 2.1 (made with Biorender.com) First, it was first

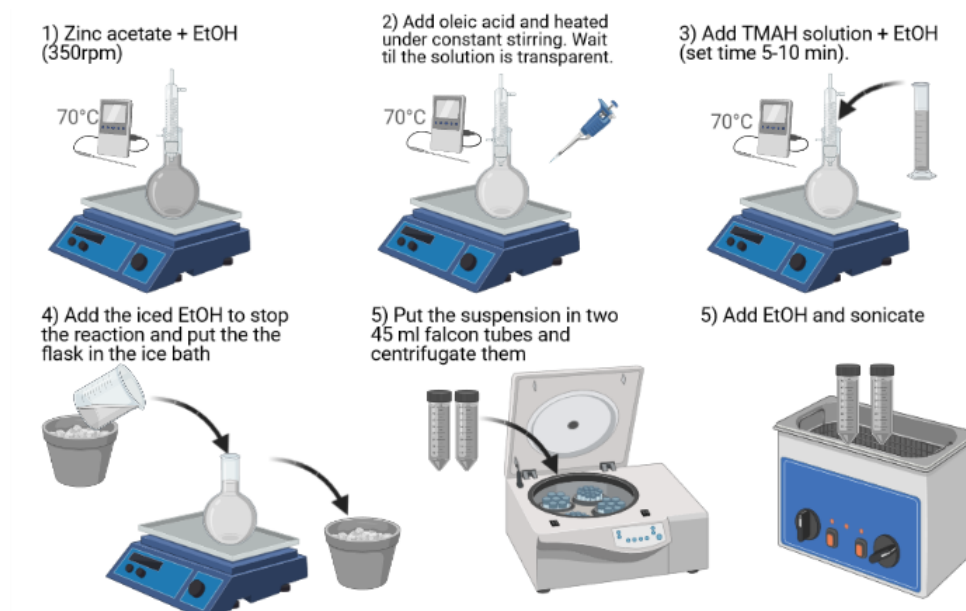


Figure 2.1: Coprecipitation method to synthesize nanoparticles

necessary to get out the oleic acid from the fridge, to unfreeze it, and to switch on the ice machine. Zinc acetate and TMAH were put in vacuum for 30 minutes and 40 ml of ethanol were put in the ice to freeze. We weighted the zinc acetate (0,5268g) and we put it in the balloon flask with 40 ml of ethanol. The flask was put on the stirrer at 350 rpm at 70°C. For the Gadolinium doped nanoparticles, we also weighted the gadolinium acetate (96,3g) and we put it also in the flask. After reaching the temperature, we put the oleic acid (140 μ l) in the flask. In the meantime, we weighted the TMAH (0,522g) to dissolve it first in 1,052ml of bidistilled water and then added to 10 mL of absolute ethanol and rapidly we put this TMAH solution in the reaction mixture under stirring. After 5 minutes under stirring (or 10 minutes for doped nanoparticles), 50 mL of ice-cold ethanol was added and then the flask was put in an ice-bath to cool it. After some minutes, the colloidal suspension was divided in two 45ml falcon tubes and the nanoparticles were collected by centrifugation (1000 xg for 10 minutes) and then were washed with ethanol twice by performing centrifugation and redispersion processes.

2.2 Functionalization method

It is known that the size and the surface chemistry of nanoparticles affect their accumulation in living organs and their internalization into cells. ZnO nanoparticles expose neutral hydroxyl groups which control the surface charge modifications [27]. Under physiological pH values, ZnO nanoparticles, which have an isoelectric point at pH 9-10, take a positive charge, while cancer cells usually expose a negative charge due to the presence of anionic phospholipids, charged proteins and carbohydrates on their membrane [27]. This electrostatic attraction could improve the cellular uptake of ZnO nanoparticles. Therefore, we decided to prepare amino-propyl surface-functionalized ZnO nanoparticles to confer a predominant positive charge. At the same time, this process has been useful to promote the next coupling with the polymeric coating which showed a negative charge. To functionalize the ZnO (or doped ZnO) we used the reagent (3-Aminopropyl) trimethoxy silane (APTMS), an amino silane (179,29 g/mol). It was mainly important to disperse again the nanoparticles in the ethanol. We put the ethanol and the solution of nanoparticles in ethanol in the flask on the stirrer at 70°C with the refrigerator column. Also, the nitrogen column was put in the flask. After that, we rapidly put 12,5 μ l of APTMS (optimized by Dr. Sugata Barui) in the flask. This operation has to be done under nitrogen flow because the APTSM is really reactive. After verifying that the flask just touched the oil, we left it for 6 hours at 450 rpm. After 6 hours, we cooled down the flask with water and the solution was divided into 15 ml falcons. The flask was washed carefully with ethanol to remove eventual nanoparticles. After centrifugation at 10000xg for 10 minutes and a washing step, we collect the amino-functionalized nanoparticles. Another washing step was required before the operations of characterization to remove the unbound APTMS molecules [27]. The process is summarized in Figure 2.2 made with Biorender.com.

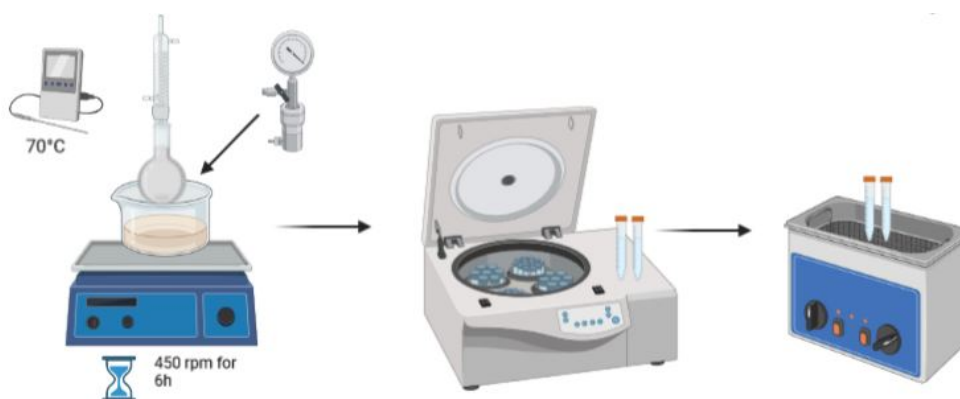


Figure 2.2: Functionalization method

2.3 Characterization Methods

2.3.1 Dynamic Light Scattering (DLS) and Zeta Potential

The first characterization of nanoparticles concerns the calculation of the nanoparticle size and of the surface charge. Dynamic Light Scattering (DLS) uses time changes of scattered light from suspended particles under Brownian motion to obtain their hydrodynamic size distribution [36]. The variations of intensity in scattered light is related with short decay intervals (τ). The intensity ACF (auto-correlation function) is calculated through the following mono-exponential equation (samples with purely monodisperse particles):

$$G(\tau) = 1 + be^{-2D_t q^2 \tau} \quad (2.4)$$

b =constant dependent upon optical settings of the instrument D_t =translational diffusion coefficient and q =scattering vector which can be expressed by the equation (2).

$$|q| = \frac{4\pi\eta_0}{\lambda_0 \sin(\theta/2)} \quad (2.5)$$

η_0 =refractive index of the solvent, λ_0 =wavelength in vacuum and θ = scattering angle. The autocorrelation functions in DLS are calculated fitting the data and from the Equation (2.4) it's possible to derive D_t [37]. The hydrodynamic radius (R_H) of solid spherical particles can be obtained by Stokes-Einstein equation (Eq. (2.6)) [37]:

$$D_t = \frac{k_B T}{6\pi\eta R_H} \quad (2.6)$$

Where k_B =Boltzmann constant= $1,38064852 \times 10^{-23}$ J/K, T =temperature, η =absolute viscosity and R_H =hydrodynamic radius. The instrumentation of DLS is composed by three main components: laser, sample and the light detector. The laser provides a coherent beam of monochromatic light and there is an attenuator to change the power [37]. The sample should be clean and homogeneous, without any precipitation [37]. The minimal volume required for the test changes with the model. Modern DLS instruments are provided of APD (avalanche photodiode detectors) that are positioned at 173° angle to detect backscattering, to exclude excess scattered light, and to increase the illuminated sample area in the cuvette. In the oldest versions the detector is placed at 90° angle [37].

The Zeta Potential (ZP) is the potential at the slipping/shear plane of a colloid particle moving under electric field [37]. When a charged particle is dispersed, an adsorbed electric double layer (EDL) is developed on its surface. The inner layer is made mostly of ions/molecules with opposite charge with respect to the particle (Stern layer). Beyond Stern layer there is a diffuse layer containing both negative

and positive charges [37]. During electrophoresis the particle with adsorbed EDL shifts to the electrodes with the slipping plane becoming the interface between the mobile particles and dispersant. The ZP is the electrokinetic potential at this slipping plane [37]. The ZP can not be obtained directly, but it is derived from electrophoretic mobility (μ_e) of charged particles under an applied electric field.

$$\mu_e = \frac{V}{E} \quad (2.7)$$

Where V=particle velocity ($\mu\text{m/s}$), and E=electric field strength (Volt/cm). The ZP is calculated by the Henry's equations:

$$\mu_e = \frac{2\epsilon_r\epsilon_0\zeta f(K_a)}{3\eta} \quad (2.8)$$

Where ϵ_r =dielectric constant, ϵ_0 =permittivity of vacuum, ζ = Zeta Potential, $f(K_a)$ = Henry's function and η =viscosity at experimental temperature.

The instrumentation of ZP measurement is represented in Figure 2.3. The laser beam is divided into two: one beam is directed to the sample and the other one represents the reference [37]. The scattered light from the sample is combined with the reference beam to obtain the Doppler shift. The magnitude of particle velocity (V) is derived from the Doppler shift and then the ZP is measured through the series of mathematical equations [37].

In this work, we decided to evaluate the hydrodynamic sizes and the polydispersity indexes (PDI) of the nanoparticles in ethanol and in neutral water at pH 7, while the zeta potentials are evaluated only in neutral water at pH 7. Firstly, we calculated the concentrations of the nanoparticles in ethanol as follows: we weighted empty eppendorfs and put inside them 500 μl of nanoparticles solution and let the ethanol evaporate at room temperature. When the ethanol was completely evaporated, we weighted again the eppendorfs and we calculated the concentration of the nanoparticles, considering the starting volume and the weight's difference. All the DLS and zeta potential measurements were carried out at room temperature at a concentration of the samples of 100 $\mu\text{g/mL}$ and each sample was sonicated for 10 minutes before the acquisition. All the measurements were carried out with a Zetasizer Nano ZS90 (Fig. 2.3).



Figure 2.3: Zetasizer Nano ZS90

2.3.2 X-Ray Diffraction (XRD)

The X-Ray Diffraction (XRD) is a technique useful to obtain information about the crystalline structure of the tested material. Considering the position of the peak, it is possible to evaluate the lattice parameters, the chemical composition, and to make quantitative and qualitative analysis [38]. The XRD is based on the principle of X-ray diffraction: it occurs between photons and electrons that surround the nucleus. So, the radiation is scattered and, considering the nature of the structure, the scattering can be destructive or constructive. The constructive one is produced when the light is scattered by periodic array with long-range order, and it occurs at specific angles [39]. Materials with no long-range order do not produce any significant peaks in the pattern [39]. The XRD has a lot of advantages such as non-destructive nature, high sensitivity, fast speed, good resolution, and easy sample preparation. The only problem is due to the use of harmful radiation employed during the analysis [39]. The instrumentation is schematically reported in Figure 2.4 and is composed by:

- X-ray source: the intensity of the radiation and the size of the beam produced by the anode are the most important parameters in the X-ray generation. There is a tungsten filament that produces the acceleration of the electrons and therefore the generation of the photons. This acceleration has a voltage between 20 kV and 60kV. Only the 1% of the energy is used to produce X-rays while the other remaining part is dissipated as heat. There is also a continuous water cooling of the anode [38].
- Primary and secondary optics: The primary optics is composed by some optical devices to obtain the best signal intensity and wavelength. There are different optical devices employed in the analysis. For example, Göbel

mirrors consist in a series of strongly and weakly scattering materials that constitutes the monochromator available with different wavelength. Another example are the Soller slits composed by 20-40 thin plates of metals with high absorption, piled in parallel with a small gap with a defined length, used to modify the divergence in vertical or horizontal direction [38]. Secondary optics is constituted by devices placed between the sample and the detector and are used to define the diffracted beam [38]. They are used to filter or reduce the radiation or to remove a specific wavelength.

- Goniometer: it allows the movement of the X-ray source, the sample and the detector. There are two major types of goniometers: θ/θ (the sample is fixed while the detector and the X-ray sources are in movement) and $\theta/2\theta$ (the source is fixed while the detector and the sample are moving) [38].
- Sample holder.
- Detector: its purpose is to convert the impinging X-ray photons in another signal to analyse it. There are some types of detectors based on different technologies, such as gas detectors (based on the ionization of a gas by the photons producing voltage pulses), or solid detectors (that convert the photons' energy in visible light) [38]. Another classification is based on the size and the active detecting area, so there are zero-dimensional detectors, point detectors, and one-dimensional detectors which have a large active detecting area in 2θ [38].

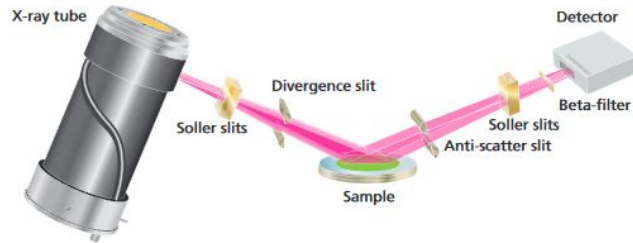


Figure 2.4: Classic diffractometer setup in Bragg-Brentano geometry with components for reflection measurement [40]

The constructive interference is satisfied by the Bragg-Brentano law:

$$2d\sin(\theta) = n\lambda \quad (2.9)$$

This law establishes that the incidence angle θ is equal to the detection angle so the peaks are observable only when the scattering is parallel to the sample

surface. Another possibility concerns a very low angle of incidence and an increased detection angle (Thin-Film technique), so this makes possible to obtain an higher sensitivity and to analyse thin films. To evaluate the means size of the crystals, the Deybe-Sherrer formula is used:

$$D = \frac{K\lambda}{\Delta_{2\theta}\cos(\theta)} \quad (2.10)$$

$K \approx 0,9$ and it is a factor that considers the shape of the grain, $\Delta_{2\theta}$ = distance in radiant between the point at half of the maximum intensity (FWHM), λ =wave-length and θ =angle of incidence.

We performed the XRD analysis at room temperature using a Panalytical X'Pert diffractometer (Fig. 2.5) in θ - 2θ Bragg-Brentano configuration with a source of Cu- $K\alpha$ radiation. The settings were $\lambda=1.54059 \text{ \AA}$, 40 kV and 30 mA. The aim was to evaluate the crystalline structure of the samples (ZnO nanoparticles, ZnO doped nanoparticles and functionalized ones). It is known that zinc oxide has a hexagonal wurtzite structure, with unit cell parameters $a = b = 3.253 \text{ \AA}$ and $c = 5.209 \text{ \AA}$ [41]. The measurements were all made in 2θ range of 20° - 80° with a step size of 0.02° and an acquisition step time of 100s. The suspensions of nanoparticles were placed drop by drop on the silicon wafers. The FWHM was obtained using the fitting functions of the peaks in Origin software (using Gauss peak function). To calculate the mean size of the crystallite structure, the Deybe-Sherrer equation was used.



Figure 2.5: Panalytical X'Pert diffractometer

2.3.3 Field Emission Scanning Electron Microscopy (FESEM)

To obtain information about the shape and the size of the synthesized nanoparticles, we performed field emission scanning electron microscopy (FESEM). FESEM is a microscope that works with a source which emits electrons with negative charge instead of light [42]. Electrons are accelerated by an electrical field gradient. This primary electron beam, inside the high vacuum column, is focused and deflected by electronic lenses to reach the sample [42]. A detector captures the secondary electrons and generates an electron signal [42]. The signal is converted in a digital image useful for the simulation [42]. A schematic representation of the FESEM components is reported in Figure 2.6. We prepared four samples for the FESEM

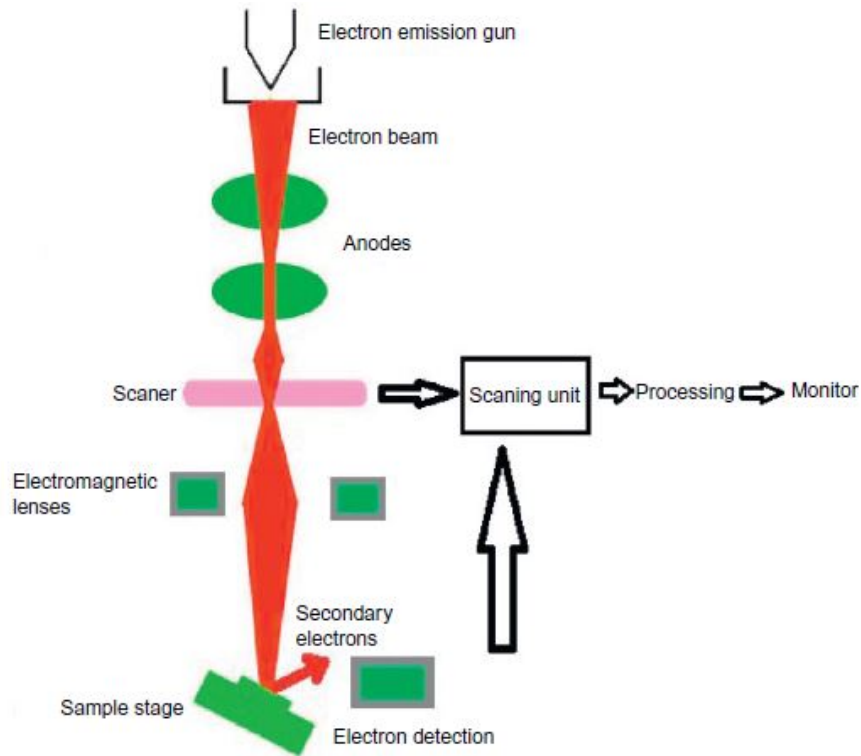


Figure 2.6: FESEM schematic components

analysis. We deposited drop by drop the NPs solution on the silicon wafer and we performed the analysis. The samples were: ZnO NPs, ZnO-Gd NPs, and amine-functionalized ZnO and ZnO-Gd NPs. The instrument used is reported in Figure 2.7.



Figure 2.7: FESEM instrumentation

2.4 Nanoprecipitation method to coat the ZnO nanoparticles

ZnO nanoparticles (and Gd-doped ones) were coated with a polymer shell using the procedure described in Figure 2.8. Briefly, 20 μg , 50 μg and 100 μg of ZnO or ZnO-Gd NPs were suspended in chloroform together with 1 mg of the polymer (proprietary polyurethane, PU) and vortexed to homogenize the suspension. The solvent was completely evaporated to obtain a composite polymer/ZnO or polymer/ZnOGd film, which was resuspended in 1ml of acetonitrile and thoroughly homogenized by vortexing the solution. The solution was then dropped into 2 mL of water containing a mixture of phospholipids (200 μg of DSPE-PEG and 240 μg of EGG-PG) and maintained under stirring at 60°C for several minutes. Nanoparticles formed spontaneously by nanoprecipitation. The nanoparticle suspension was then cooled to room temperature by adding 1 mL of distilled water, and particles were collected by centrifugation 3200 rpm for 13 minutes on Amicon filters (cutoff 10kDa).

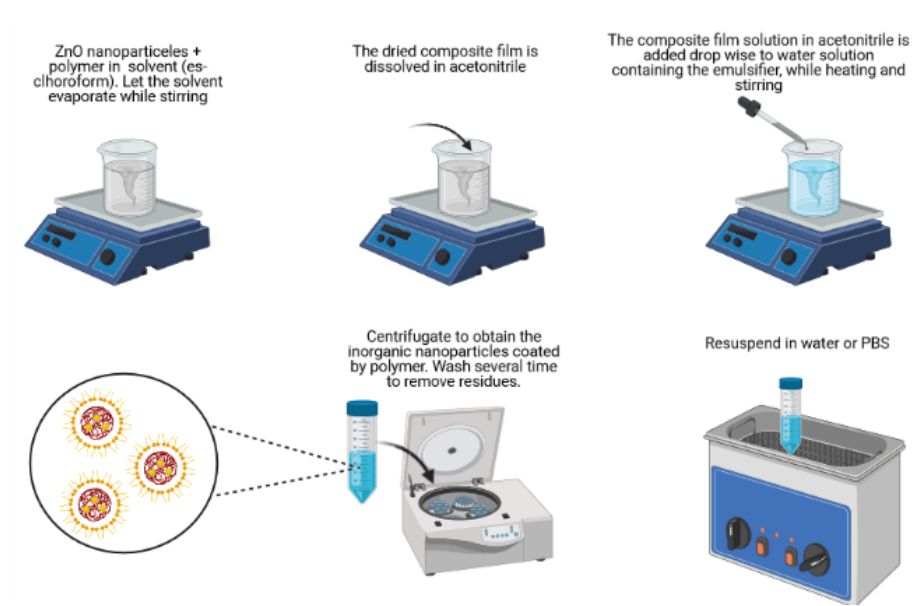


Figure 2.8: Nanoprecipitation method to coat the nanoparticle

2.5 Characterization Methods

2.5.1 Freeze-Drying

Freeze-drying allows to remove water from frozen material through sublimation [43]. Sublimation is a process in which the water passes directly from solid state to water state without the passage in fluid state. First, the sample is frozen and then it is put under vacuum to heat, so at the end we obtain dried components. Lyophilization is conducted under the triple point to enable sublimation of ice. The process consists in three steps (Fig. 2.9) [44]:

- Freezing: The sample is frozen and it's important to cool the material under its eutectic point (where solid and liquid component coexist). Usually, the temperature used is between -50°C and -80°C [44].
- Primary drying: In this phase, the sublimation starts and the 95 % of the water is sublimated. This is a slow step because if the heat is too high, the structure of the material could be modified. To control the pressure, a partial vacuum is applied [44].
- Secondary drying: It is useful to remove unfrozen water molecules. At the end, the vacuum is removed with an inert gas, such as nitrogen, and the material is dried with a low content of residual water (around 1 % - 4 %) [44].

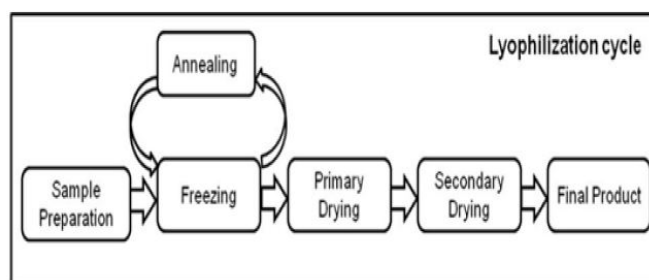


Figure 2.9: Freeze-drying process [44]

The instrumentation is composed by a vacuum pump, a condenser, and a reservoir for the dried substances [44]. The lyophilization is useful in pharmaceutical and biotechnology fields to store materials for more time (for example vaccines or other injectables). The instrument used for the freeze-drying was the ScanVac CoolSafe Freeze Dryer (Fig. 2.10).

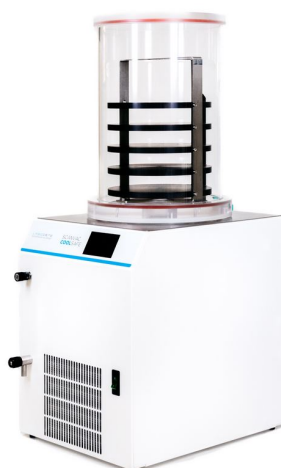


Figure 2.10: ScanVac CoolSafe Freeze Dryer

The percentage yield was calculated for the formulation with a quantity of 50 μg of zinc oxide. The samples were frozen and put in the freeze drier over night. With the weight of the obtained powder, it is possible to calculate the percentage yield (Eq. 2.11).

$$\text{Percentage Yield} = \frac{\text{Weight of formulations}}{\text{Weight of reagents}} \times 100 \quad (2.11)$$

Where the weight of reagents is calculated as the sum of the weight of the ZnO nanoparticles (50 μg) and of the polymeric coating (1 mg).

2.5.2 Transmission Electron Microscopy (TEM)

Transmission Electron Microscopy (TEM) is useful to analyse structures with characteristic dimension less than 100 nm [45]. The principle of operation is based on the diffraction that occurs when an electron beam interacts with the sample [46]. The electron beam is emitted by an electron gun, and it is focused by metal holes and electromagnetic lens in the column of TEM [45]. Only the electrons with a specific energy in a small range can pass and the transmitted electrons are applied to a specimen placed in a sample holder in the column. The thickness of the specimen should be at most around 100 nm to allow the passage of the electrons, while other features such as concentration could influence the transmission [45]. Then there are two electromagnetic lenses after the specimen that magnify the transmitted electrons and at the end the electrons are projected on a phosphor screen to obtain the visible form of the image. With this system, it is possible to have high resolution in nanoscale using electrons with short wavelength. The components of the TEM can be observed in Figure 2.11. For TEM analysis the samples were suspended in water and analyzed at the Joint Research Facility Centre in Ispra.

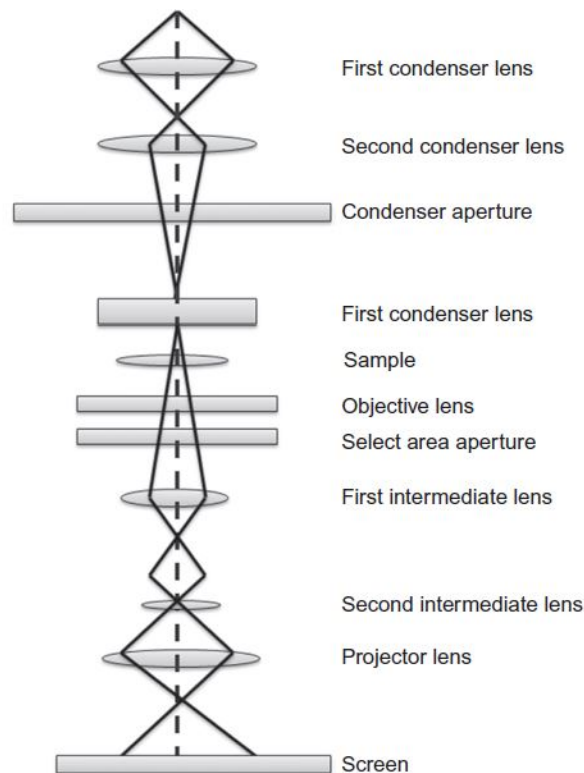


Figure 2.11: Components of TEM [46]

2.5.3 Quantification of ZnO loading

The amount of ZnO loaded inside the polymeric coating was calculated by Graphite Furnace Atomic Absorption Spectroscopy (GF-AAS). The samples were prepared to obtain a 10 mL solution with an approximate concentration of 2ppm of nanoparticles in water. The samples were sent to an external facility to be analyzed with GF-AAS. All the samples were mineralized under acidic conditions and the Zn content was determined following the EPA method 289.1. From these concentration, the amount of ZnO NPs present in the nanoconstructs was back-calculated (Eq. 2.12)

$$\% \text{ Of Loaded ZnO} = \frac{\text{Amount of ZnO in suspension}(\mu\text{g})}{\text{Theoretical quantity of ZnO supplied}(\mu\text{g})} \times 100 \quad (2.12)$$

2.5.4 Viability Assay

The viability assay has been used to evaluate the cytotoxicity of the synthesized nanoparticles in pancreatic adenocarcinoma cells (BxPC-3 cell line). Cells were cultured in RPMI + 10 % of fetal bovine serum and 1 % pen/strep. Cells were plated at 8000 cells/well (100 μL) in 96 well plates, allowed to attach, and treated with 4 different concentrations of ZnO nanoparticles, ZnO-PU nanoparticles and empty PU nanoparticles (50 $\mu\text{g}/\text{mL}$ (stock), 25 $\mu\text{g}/\text{mL}$, 10 $\mu\text{g}/\text{mL}$ and 5 $\mu\text{g}/\text{mL}$) in triplicate for 24 and 48 hours. To determine cell viability, cells were analyzed with CellTiter-Glo Luminescent Cell Viability Assay. Briefly, 100 μL of reagent were added to each well and the plate was shaken for 10 minutes to allow the generation of a luminescent signal proportional to the number of viable cells. The content of each well was then transferred to white opaque multiwell plates and luminescence was read on a SynergyTM HTX Multi-Mode Microplate Reader (Fig. 2.12). The results were referred to the viability of wells containing only cells. The same procedure has been followed for the doped nanoparticles.



Figure 2.12: Schematic representation of viability assay

2.5.5 Fluorescence Activated Cell Sorter (FACS)

Fluorescence Activated Cell Sorter (FACS) is a powerful tool useful to evaluate the cellular condition, using a measure of a single or multiple fluorescent signals and of additional scatter light signals which provide a first characterization of the tested cells [47]. Different fluorochromes can be used, therefore it is necessary to interpret the obtained signals in the correct wavelength spectrum [47]. The instrumentation is composed by a laser, which excites the cells and the associated fluorochromes, a bandpass filter, which allows the passage of only some fluorescence signals with specific wavelengths, and a detector, which collects the signals [47]. To assess cell internalization of ZnO and ZnO-PU NPs, the inorganic NPs were labelled with Atto 647 dye which emits at 667 nm. To achieve this, 400 μl of dye solution (2 mg/mL) were added to 200 μg of ZnO nanoparticles stirred at 200 rpm overnight. Afterwards, NPs were washed twice and collected. BxPC-3 cells were plated at 200.000 cells/well in 6 well plates, allowed to attach for 24 hours, and treated with ZnO and ZnO-PU NPs at a ZnO concentration of 20 $\mu\text{g}/\text{mL}$ in triplicate for 24 hours. FACS analysis was performed using the Guava® easyCyte™ Flow Cytometer (Figure 2.13). The procedure is schematically reported in Figure 2.14.



Figure 2.13: Guava® easyCyte™ Flow Cytometer

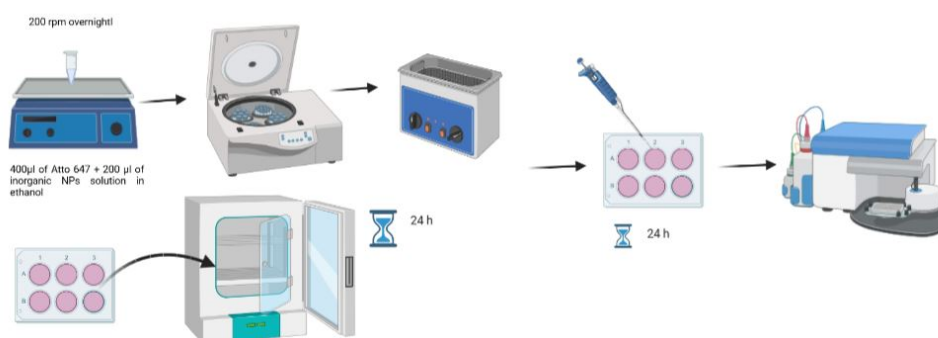


Figure 2.14: NPs preparation for FACS analysis

2.6 Drug encapsulation

GEM-doped ZnO and ZnO:Gd nanoparticles were prepared as follows: 200 μg of nanoparticles solution in ethanol was centrifuged at 14000 rpm for 10 minutes to obtain the NPs pellet, followed by addition of 400 μl of drug stock solution (1 mM in bidistilled water). The solution was put on the stirrer for 2 hours at 200 rpm. Two control samples were also prepared: a negative control (bidistilled water) and a positive control (1 mM drug solution). After two hours, the samples were centrifuged again and the corresponding supernatant with the controls were put in a quartz micro-plate (triplicate of 100 μl) and analyzed with the UV-Vis spectrophotometer. The difference between the measured values and the negative control represented the drug which was not encapsulated in the nanoparticles. From the calibration curve, we derived the concentration of the drug in the samples and obtained the concentration of the encapsulated drug from the difference between the concentration of the sample and of the positive control. The quantity of GEM encapsulated in the NPs was obtained, knowing the weight of the NPs, the volume of the supernatants and the molecular weight of the drug.

2.6.1 Viability Assay - Drug-encapsulated Nanoparticles

The viability of cells treated with GEM-NPs was tested as described before, after incubating the cells with 25 μg , 10 μg and 5 μg of GEM-ZnO and GEM-ZnO-PU NPs for 24 hours.

Chapter 3

Results and Discussion

3.1 Uncoated Nanoparticles

3.1.1 Dynamic Light Scattering (DLS) and Zeta Potential

Table 3.1 reports the concentrations of the inorganic nanoparticles solutions calculated as reported in Chapter 2 Section 2.3.1.

Sample	Concentrations (mg/ml)
ZnO Nanoparticles	2,8
ZnO-Gd Nanoparticles	3,4
Amine-Funct ZnO Nanoparticles	5,2
Amine-Funct ZnO-Gd Nanoparticles	5,4

Table 3.1: Concentrations of synthesized nanoparticles

Figure 3.1 and Tables 3.2 and 3.3 report the average results of size and PDI measured for ZnO NPs, doped ZnO and the Gd-doped counterparts evaluated both in water and in ethanol. All NPs samples showed a good size distribution, ranging from 147 nm to 181 nm in water and from 133 nm to 174 nm in ethanol, and appear well monodisperse, as demonstrated by the low PDI values (ranging from 0,02 to 0,03 in water and from 0,007 to 0,04 in ethanol) and by the narrow size distribution (Figures 3.2 and 3.3)

Sample	Z-ave Size in water (nm)	PDI
ZnO Nanoparticles	$167 \pm 4,$	$0,12 \pm 0,02$
ZnO-Gd Nanoparticles	$147 \pm 0,3$	$0,09 \pm 0,03$
Amine-Funct ZnO Nanoparticles	$182 \pm 3,3$	$0,2 \pm 0,03$
Amine-Funct ZnO-Gd Nanoparticles	$176 \pm 3,2$	$0,14 \pm 0,02$

Table 3.2: Hydrodynamic sizes and polydispersity indexes (PDI) in water.

Sample	Z-ave Size in ethanol (nm)	PDI
ZnO Nanoparticles	174 ± 5	$0,07 \pm 0,04$
ZnO-Gd Nanoparticles	159 ± 2	$0,09 \pm 0,01$
Amine-Funct ZnO Nanoparticles	$133 \pm 1,3$	$0,09 \pm 0,007$
Amine-Funct ZnO-Gd Nanoparticles	$134 \pm 1,3$	$0,09 \pm 0,011$

Table 3.3: Hydrodynamic sizes and polydispersity indexes (PDI) in ethanol.

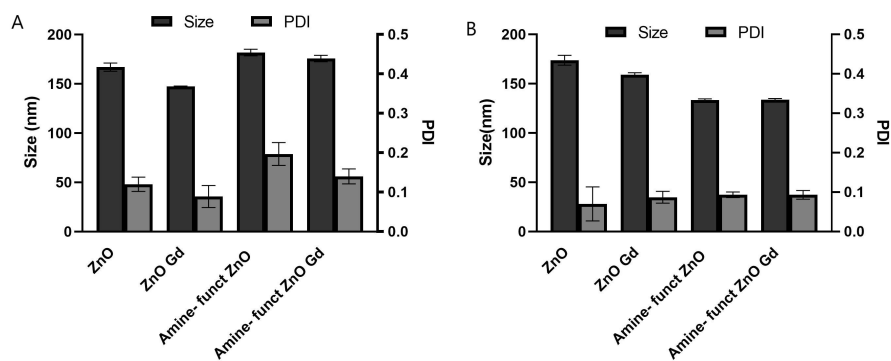


Figure 3.1: Hydrodynamic sizes and polydispersity indexes (PDI) in (A) water and (B) in ethanol

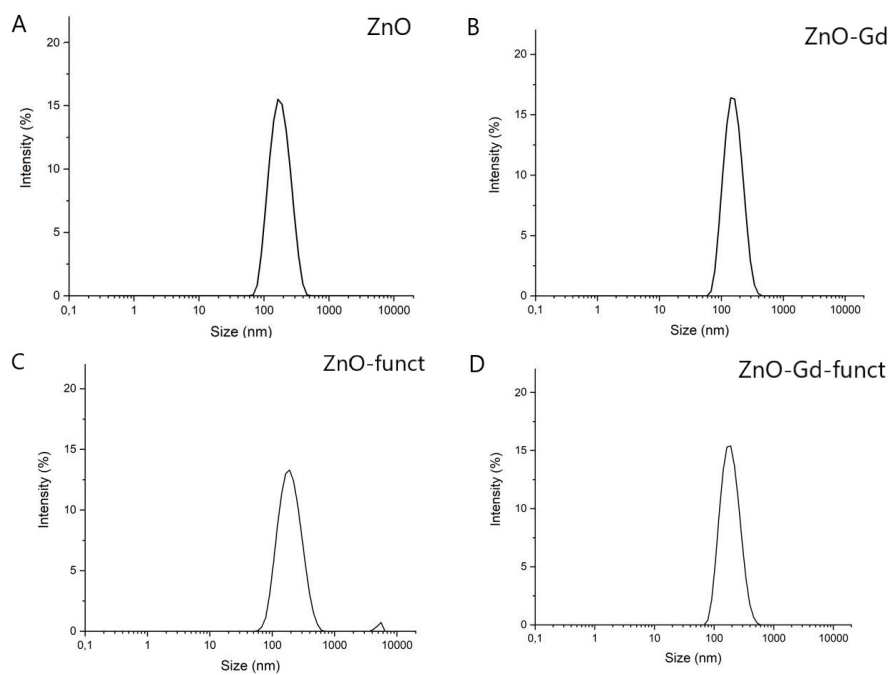


Figure 3.2: DLS measurement in intensity % of (A) ZnO, (B) ZnO-Gd, (C) amine-functionalized ZnO and (D) ZnO-Gd nanoparticles in water

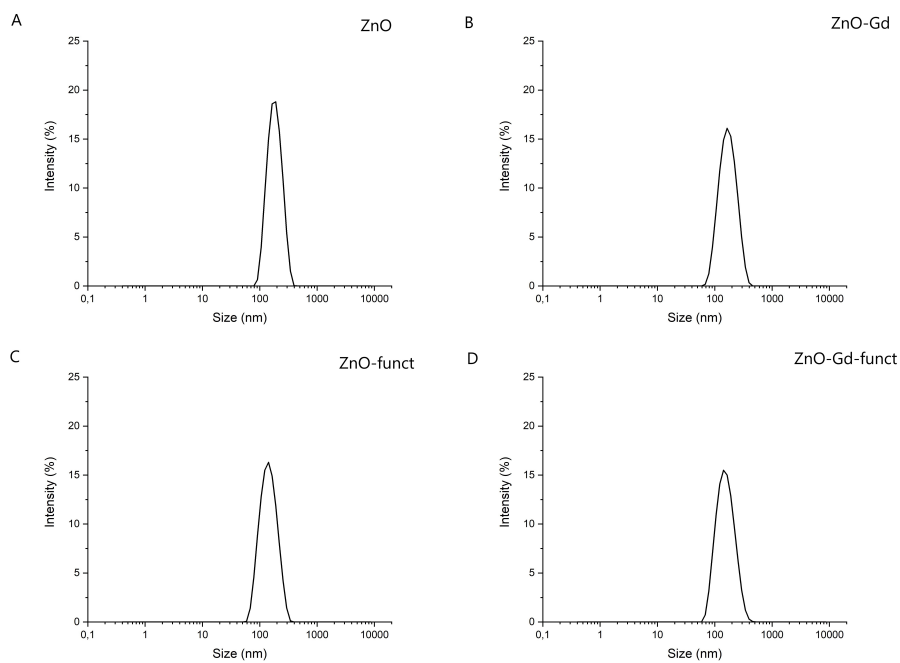


Figure 3.3: DLS measurement in intensity % of (A) ZnO, (B) ZnO-Gd, (C) amine-functionalized ZnO and (D) ZnO-Gd nanoparticles in ethanol

The zeta potential measured for all inorganic NPs is reported in Figure 3.4. All NPs showed positive values, according to the positive charge of ZnO [27]. A slightly higher zeta potential was observed for the amine-functionalized samples (of 34 % for ZnO NPs and of 13 % for Gd-dopen NPs). This was attributed to the positive charge of the amino groups and can be considered a further confirmation of the successful modification of the ZnO core

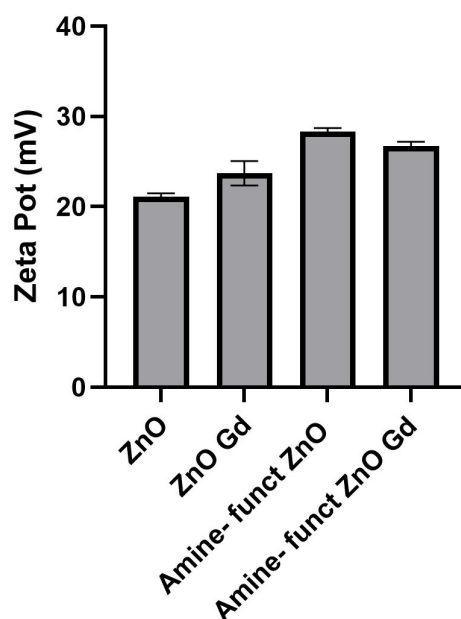


Figure 3.4: Zeta Potential of all inorganic NPs

3.1.2 X-Ray Diffraction (XRD)

The XRD patterns obtained for each sample are reported in Figure 3.5.

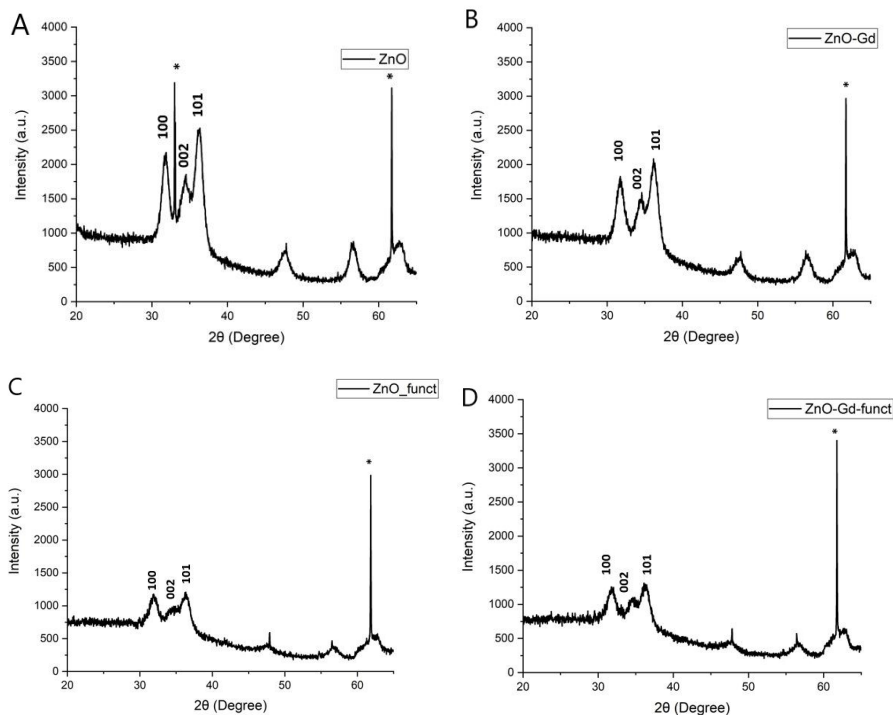


Figure 3.5: X-ray diffractometer of (A) ZnO, (B) ZnO-Gd nanoparticles and amine-functionalized (C) ZnO and (D) ZnO-Gd nanoparticles

The peaks can be classified as reported by the Joint Committee on Powder Diffraction Standards-International Centre for Diffraction Data (JCPDS-ICDD) database (card no- 89-1397) (Table 3.4).

The positions of the peaks (100), (002) and (101) in the patterns (Fig. 3.5) are characteristic for the zinc oxide structure, while the peak signed with an asterisk (*) is due to the silicon wafer. Diffraction peaks related to impurity were not observed in the XRD patterns, and this confirms the high purity of the synthesized products [48] as well as the absence of secondary phases due to the doping. The $\Delta 2\theta$ values have been obtained using the Gaussian function on Origin software and the average particle sizes have been determined from full width at half maximum (FWHM) of the diffraction peaks [29] using the Debye-Scherrer equation (Eq. 2.10) and are reported in Tables 3.5-3.8 for ZnO, doped ZnO, amine-functionalized ZnO and doped ZnO samples respectively. The variations of $\Delta 2\theta$ suggest an increase in the lattice parameters upon doping [29]. This is due to a deformation of the crystalline structure because of the Gadolinium doping element, having an atomic size larger

$^{\circ}$	Crystallographic Plane
31,7	(100)
34,4	(002)
36,2	(101)
47,5	(102)
56,5	(110)
62,7	(103)
67,8	(112)
69,0	(201)

Table 3.4: Peaks Classification

than Zinc. Furthermore, comparing the average crystallite size of each sample (as calculated from the Debye-Scherrer equation), the Gd-doped nanoparticles have a lower size than the undoped ones. This depends on the lattice contraction due to the hydrostatic pressure usually produced by the rare elements dopants placed on the ZnO nanoparticles surface [29].

ZnO	FWHM	θ ($^{\circ}$)	D (nm)
Peak 1 - (100)	1,0488	31,78	8,816
Peak 2 - (002)	1,383	34,46	6,889
Peak 3 - (101)	0,771	36,20	12,626

Table 3.5: Debye-Scherrer diameters (nm) calculated from FWHM of the peaks with $k = 0,89$ and $\lambda = 1,54059 \text{ \AA}$ - ZnO nanoparticles.

ZnO-Gd	FWHM	θ (°)	D (nm)	$\Delta 2\theta$ (°)
Peak 1 - (100)	1,065	31,75	8,67501	0,03
Peak 2 - (002)	1,667	34,61	5,7272	-0,15
Peak 3 - (101)	0,889	36,18	10,9626	0,02

Table 3.6: Deybe-Sherrer diameters (nm) calculated from FWHM of the peaks with $k = 0,89$ and $\lambda = 1,54059 \text{ \AA}$ - ZnO-Gd nanoparticles.

ZnO-funct	FWHM	θ (°)	D (nm)
Peak 1 - (100)	1,273	31,90	7,2708
Peak 2 - (002)	1,554	34,69	6,1495
Peak 3 - (101)	0,911	36,28	10,6929

Table 3.7: Deybe-Sherrer diameters (nm) calculated from FWHM of the peaks with $k = 0,89$ and $\lambda = 1,54059 \text{ \AA}$ - ZnO-funct nanoparticles.

ZnO-Gd-funct	FWHM	θ (°)	D (nm)	$\Delta 2\theta$ (°)
Peak 1 - (100)	1,108	31,79	8,3474	0,11
Peak 2 - (002)	0,6124	34,63	15,5983	0,06
Peak 3 - (101)	0,885	36,20	10,9956	0,08

Table 3.8: Deybe-Sherrer diameters (nm) calculated from FWHM of the peaks with $k = 0,89$ and $\lambda = 1,54059 \text{ \AA}$ - ZnO-Gd-funct nanoparticles.

3.1.3 Field Emission Scanning Electron Microscopy (FE-SEM)

The FESEM images are reported in Figure 3.6 to evaluate the shape and the size of the samples. NPs show a spherical shape with a size approximately 6-10 nm in diameter, coherent with DLS results.

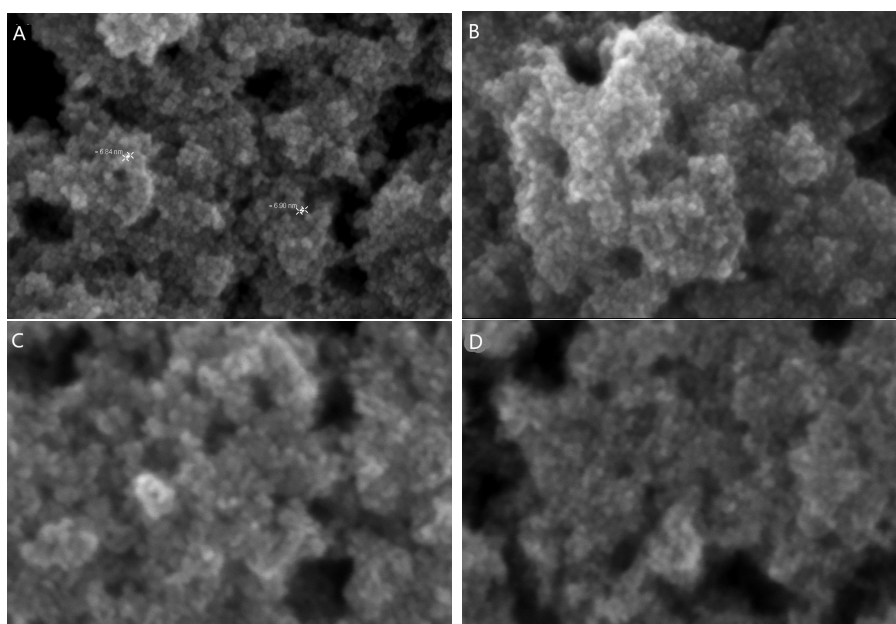


Figure 3.6: FESEM images of (A) undoped, (B) doped, (C) amine-functionalized undoped and (D) amine-functionalized doped nanoparticles

3.2 Coated Nanoparticles

3.2.1 Dynamic Light Scattering (DLS) and Zeta Potential

Table 3.9 reports the average results of size and PDI for the polymer-coated samples obtained with different amount (initial loading) of the inorganic core (20 μg , 50 μg , 100 μg). A general increase in the hydrodynamic diameter of the nanoparticles can be observed after the coating. This increase was proportional to the loaded quantity of ZnO (or Gd-doped) NPs, reaching about 10 % with the 100 μg loading. A slight increase in the polydispersity index was also observed (varying from 0,07 for the uncoated NPs, to 0,3 after coating), which may indicate the presence of aggregates, as suggested by the multimodal profile obtained by DLS (shown in Figure 3.7).

Initial Loading	Sample	Z-ave Size in water (nm)	PDI
20 μg	ZnO-PU	160 \pm 6,8	0,5 \pm 0,04
	ZnO-Gd-PU	149 \pm 4,4	0,4 \pm 0,08
	ZnO-PU-funct	160 \pm 41,8	0,4 \pm 0,1
	ZnO-Gd-PU-funct	141 \pm 25	0,5 \pm 0,81
50 μg	ZnO-PU	157 \pm 9,3	0,4 \pm 0,14
	ZnO-Gd-PU	160 \pm 13	0,3 \pm 0,04
	ZnO-PU-funct	141 \pm 27,3	0,4 \pm 0,15
	ZnO-Gd-PU-funct	141 \pm 25	0,3 \pm 0,1
100 μg	ZnO-PU	185 \pm 26,6	0,5 \pm 0,15
	ZnO-Gd-PU	187 \pm 42,2	0,5 \pm 0,2
	ZnO-PU-funct	127 \pm 15,6	0,3 \pm 0,04
	ZnO-Gd-PU-funct	161 \pm 36,4	0,4 \pm 0,14

Table 3.9: Hydrodynamic sizes and polydispersity indexes (PDI) in water for coated nanoparticles

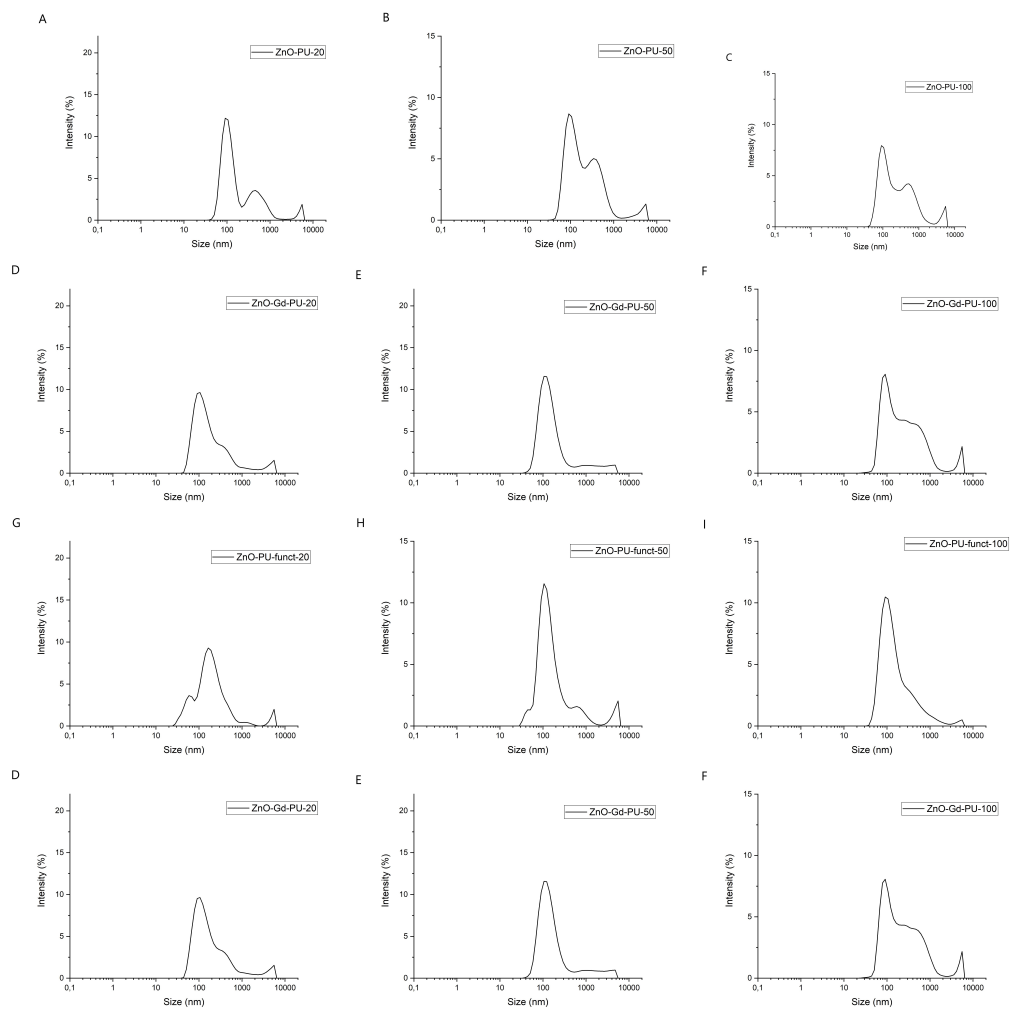


Figure 3.7: DLS Intensity profiles of PU NPs loaded with ZnO NPs at (A) 20 μg , (B) 50 μg and (C) 100 μg , PU NPs loaded with ZnO-Gd NPs at (D) 20 μg , (E) 50 μg and (F) 100 μg ; PU NPs loaded with amine-functionalized ZnO NPs at (G) 20 μg , (H) 50 μg and (I) 100 μg ; and PU NPs loaded with amine-functionalized ZnO-Gd NPs at (J) 20 μg , (K) 50 μg and (L) 100 μg

Figure 3.8 shows the comparison between size and PDI of all tested samples. The overall trend shows a size increase as compared to the pristine nanoparticles without the coating and to the polymer alone. This suggests that successful coating of the inorganic nanoparticles with the hybrid polymer/lipid shell was achieved

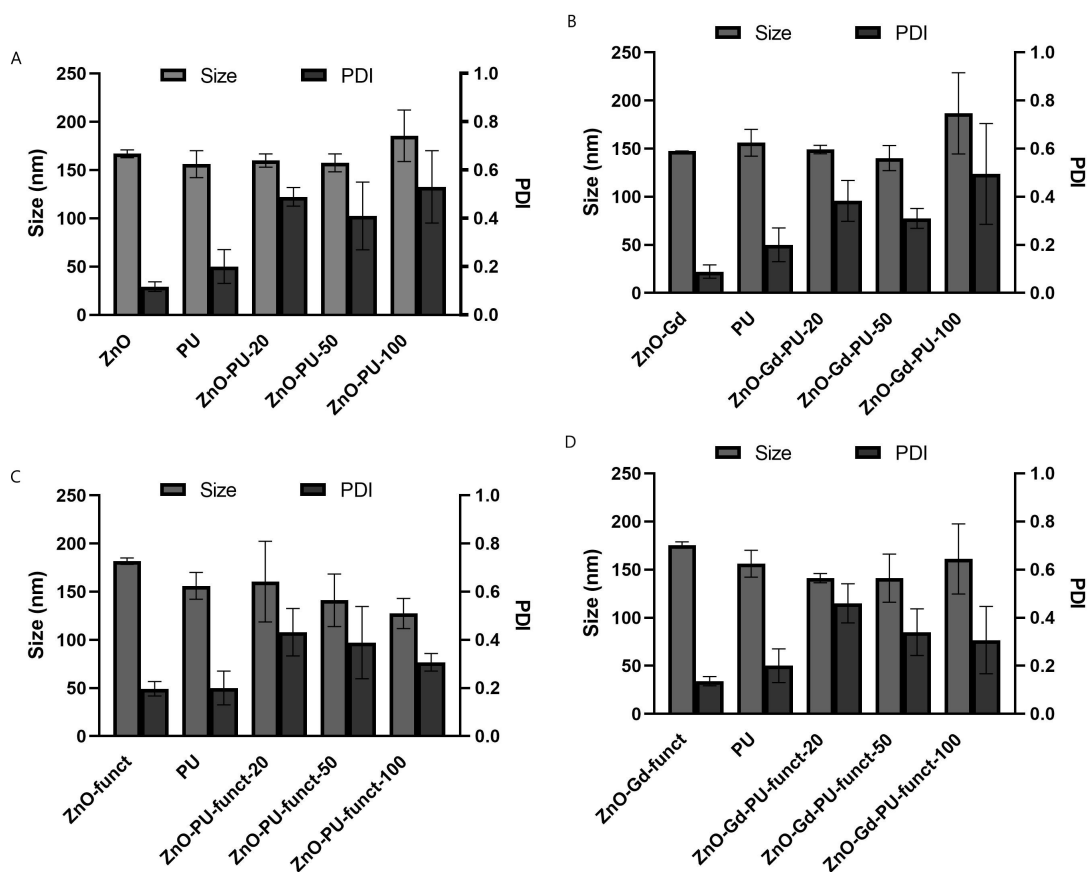


Figure 3.8: Size and PDI for coated (A) ZnO NPs, (B) ZnO-Gd NPs, (C) ZnO-funct NPs, and (D) ZnO-Gd-funct

Figure 3.9 reports the average results of Zeta Potential for the samples of ZnO, ZnO-Gd NPs and of the amine-functionalized nanoparticles coated with the polymer compared with the uncoated NPs and with the polymer. The Zeta Potential becomes negative after coating, and this means that the polymer, which has a negative charge, coats the nanoparticles because there is an inversion of the charge and effectively the amine-functionalization has improved the coupling between the inorganic nanoparticles and the polymer.

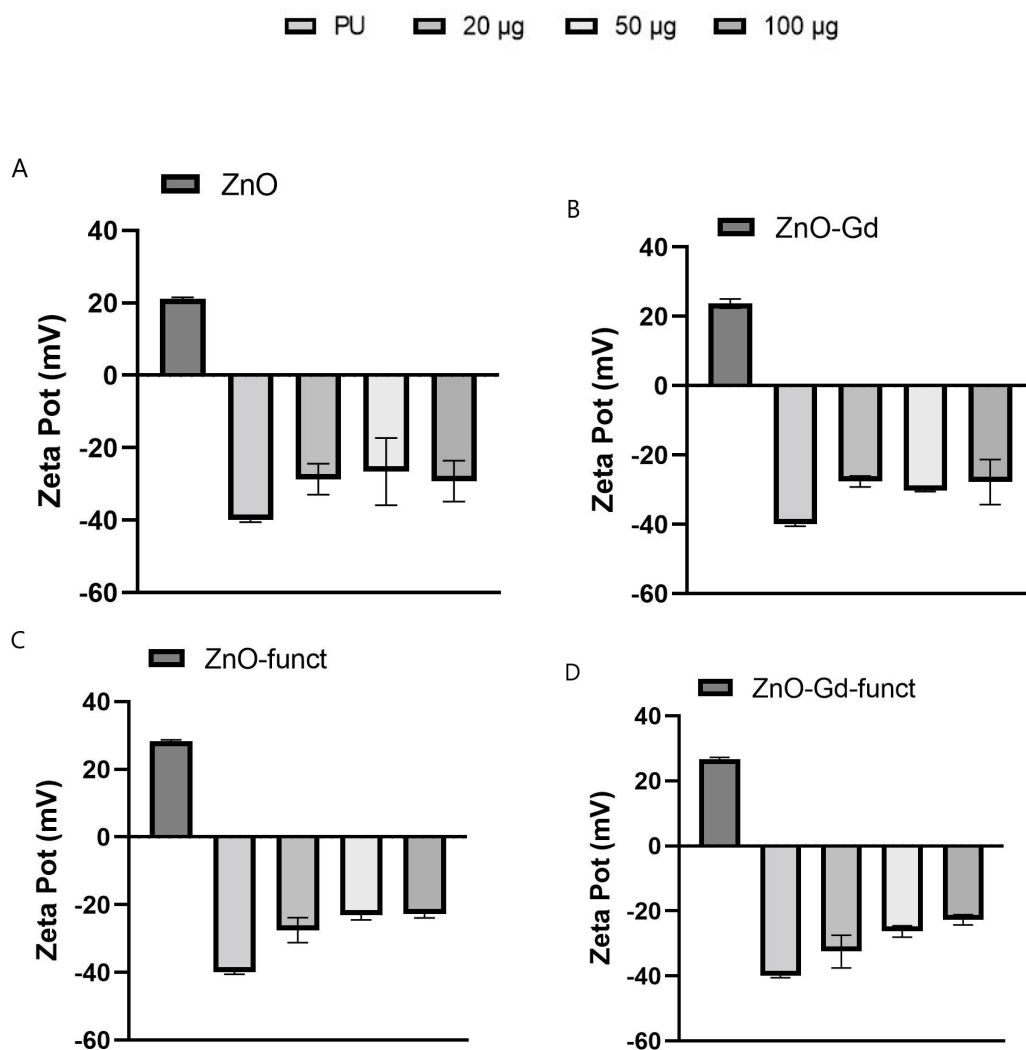


Figure 3.9: Zeta Potential for coated (A) ZnO NPs, (B) ZnO-Gd NPs, (C) ZnO-funct NPs, and (D) ZnO-Gd-funct

3.2.2 Percentage Yield

After the freeze-drying, we calculated the value of percentage yield both for ZnO nanoparticles and doped ones coated with the polymer. The theoretical yield is 1,05 mg and it is given by the quantity of nanoparticles used (50 μg) and the quantity of polymer (1 mg). The average percentage yield for ZnO NPs is 70 % and for ZnO-Gd NPs is 68,6 % and are reported in Figure 3.10. The percentage yield are good, but they show that we lose a part of the starting quantity of ZnO (or ZnOGd) after the nanoprecipitation procedure.

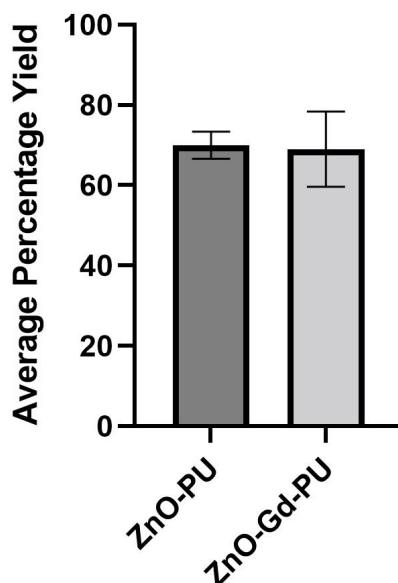


Figure 3.10: Average Percentage Yield

3.2.3 Transmission Electron Microscopy (TEM)

Figure 3.11 shows the TEM images of ZnO-PU NPs loaded with different amounts of ZNO NPs. TEM images of pristine ZnO NPs show a spherical morphology and a reproducible size, in accordance with DLS results [49]. For ZnO-PU NPs, the presence of the polymer coating can be observed in all samples, with evident signs of aggregation at the higher loading of 100 μg and 50 μg . For the 100 μg -loaded samples un-encapsulated ZnO NPs can be observed. This may indicate that this loading is too high and that the polymer does not provide sufficient coating to the inorganic core. The sample loaded with 20 μg of ZnO NPs shows good spherical morphology of the polymer NPs, with ZnO NPs clearly encapsulated.

Little evidence of un-encapsulated ZnO NPs was observed.

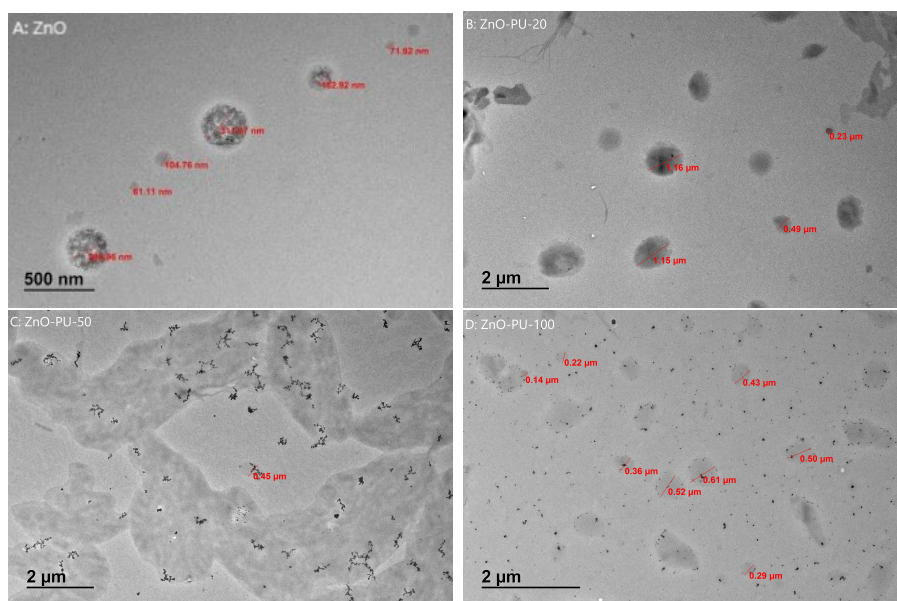


Figure 3.11: (A) TEM image of ZnO control sample; and TEM images of coated NPs loaded with (B) 20 μg , (C) 50 μg and (D) 100 μg of ZnO

3.2.4 Loading of ZnO

Figure 3.12 shows the loadings of zinc oxide obtained by the GF-AAS analysis. The analysis was conducted on a 10 mL volume solution concentrated 2 ppm. In most cases, the loading of zinc oxide is less than the starting quantity we put inside the nanoparticles, so it is possible that we have lost a part of it during the procedure of coating. This happens predominantly for NPs with higher initial loading of 100 μg and increases with a decrease of the starting loading.

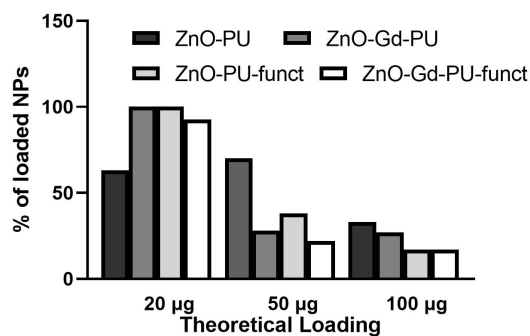


Figure 3.12: Effective loading trend in coated NPs as compared to the starting loading

3.2.5 Viability Assay

We observed the status of the treated cells (BxPC-3) after 24 hours and 48 hours to evaluate the cytotoxicity of the samples. The Figure 3.13 represents the cells used as control before the treatment.

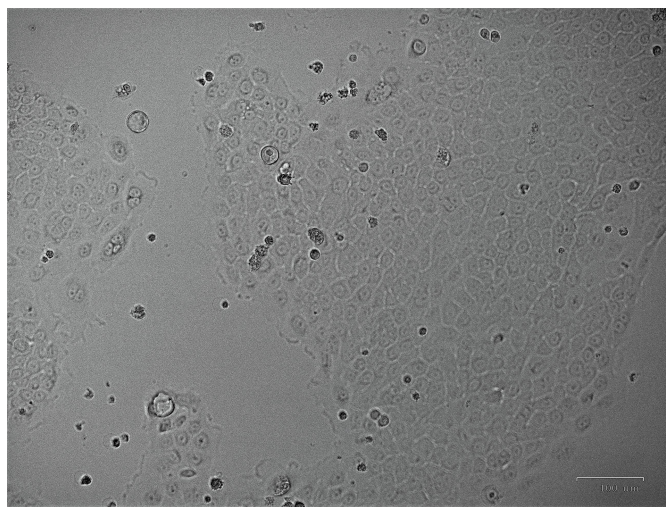


Figure 3.13: Control cells BxPC-3 before treatment

The procedure was performed both for undoped and doped ZnO nanoparticles (i.e. without PU coating) and for the coated ones using the concentrations defined in Chapter 2 Section 2.5.4.

From the graphs in Figure 3.14 we can observe that increasing the concentration of ZnO nanoparticles the number of dead cells also increases. This result is coherent

considering the intrinsic cytotoxicity of the ZnO. Adding the polymeric coating, the trend of viability changes: there is also a growing trend of cellular mortality when increasing the concentration, but it is more attenuated when compared to the bare nanoparticles. This means that effectively the polymeric coating increases the biocompatibility of the inorganic nanoparticles reducing their cytotoxicity. Comparing the two time points, there is a further decrease of the viable cells after 48 hours due to the higher internalization of the nanoparticles and the consequent cytotoxic effect.

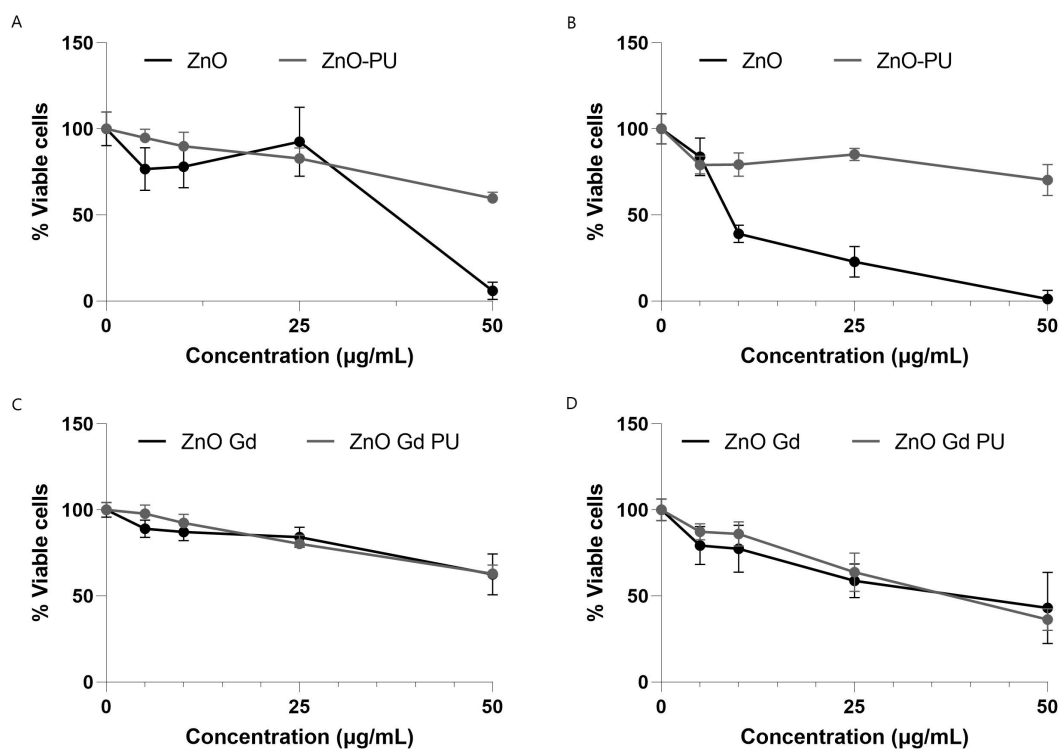


Figure 3.14: Viability assay at (A) 24h and (B) 48h for ZnO and ZnO-PU NPs; and Viability assay at (C) 24h and (D) 48h for ZnO-Gd and ZnO-Gd PU NPs

To better understand the outcomes, Figures 3.15 and 3.16 show the morphology of the cells treated with ZnO nanoparticles after 24 hours and 48 hours, while Figures 3.17 and 3.18 show treatment effect on cells treated with the coated nanoparticles. Changes in morphology and cell detachment is observed after treatment with bare ZnO NPs, confirming their intrinsic toxicity at higher dose.

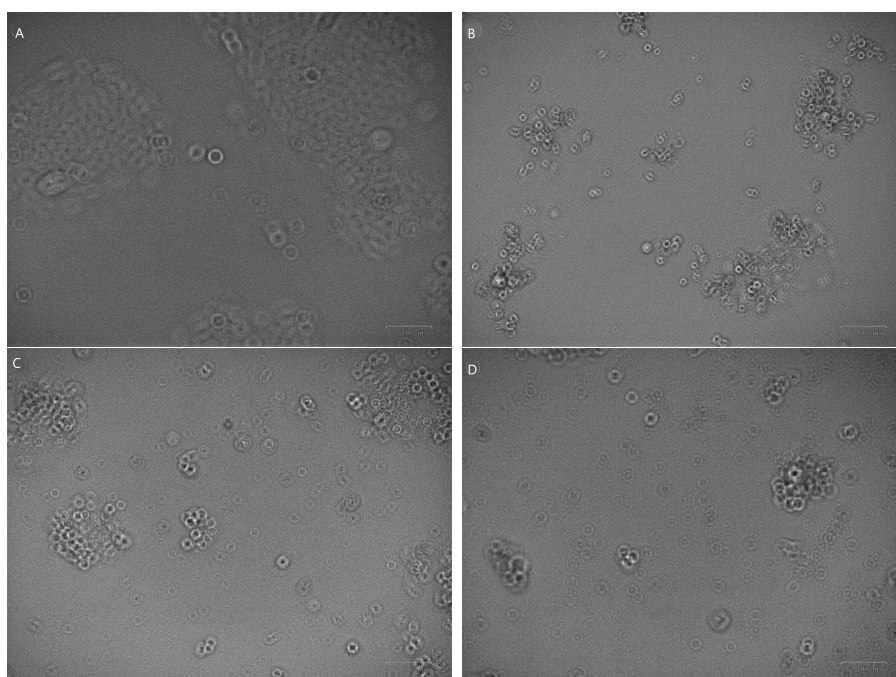


Figure 3.15: Cells treated with (a) 5 $\mu\text{g}/\text{mL}$, (b) 10 $\mu\text{g}/\text{mL}$, (c) 25 $\mu\text{g}/\text{mL}$ and (d) 50 $\mu\text{g}/\text{mL}$ of ZnO NPs after 24 hours

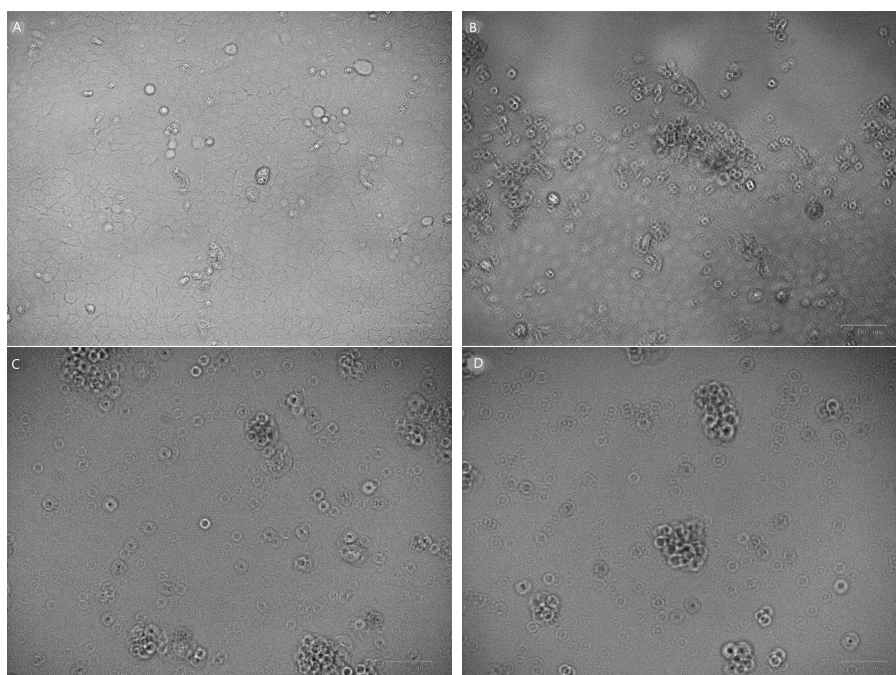


Figure 3.16: Cells treated with (a) 5 $\mu\text{g}/\text{mL}$, (b) 10 $\mu\text{g}/\text{mL}$, (c) 25 $\mu\text{g}/\text{mL}$ and (d) 50 $\mu\text{g}/\text{mL}$ of ZnO NPs after 48 hours

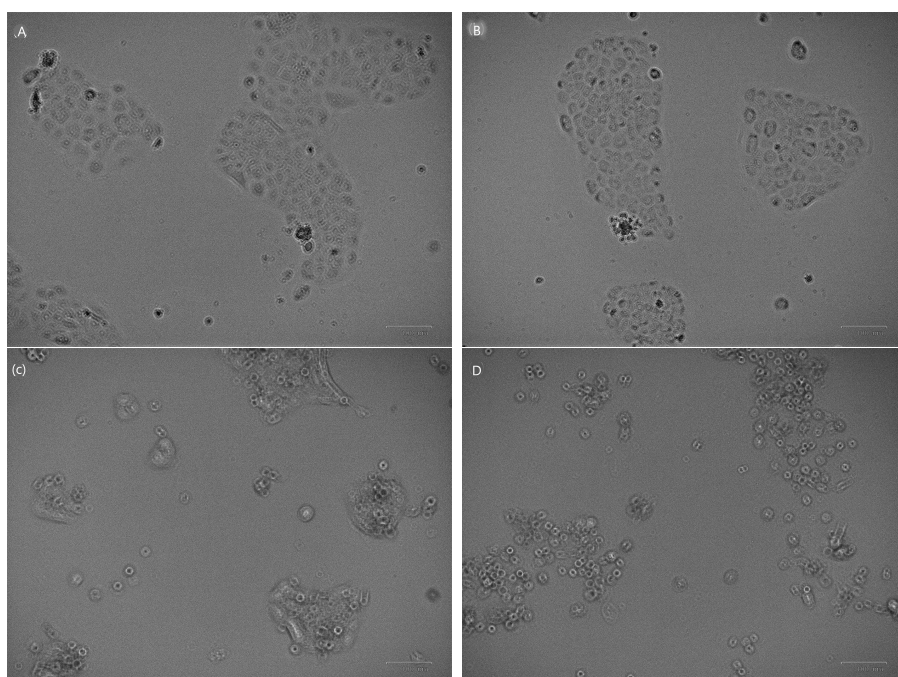


Figure 3.17: Cells treated with (a) 5 $\mu\text{g/mL}$, (b) 10 $\mu\text{g/mL}$, (c) 25 $\mu\text{g/mL}$ and (d) 50 $\mu\text{g/mL}$ of ZnO-PU NPs after 24 hours

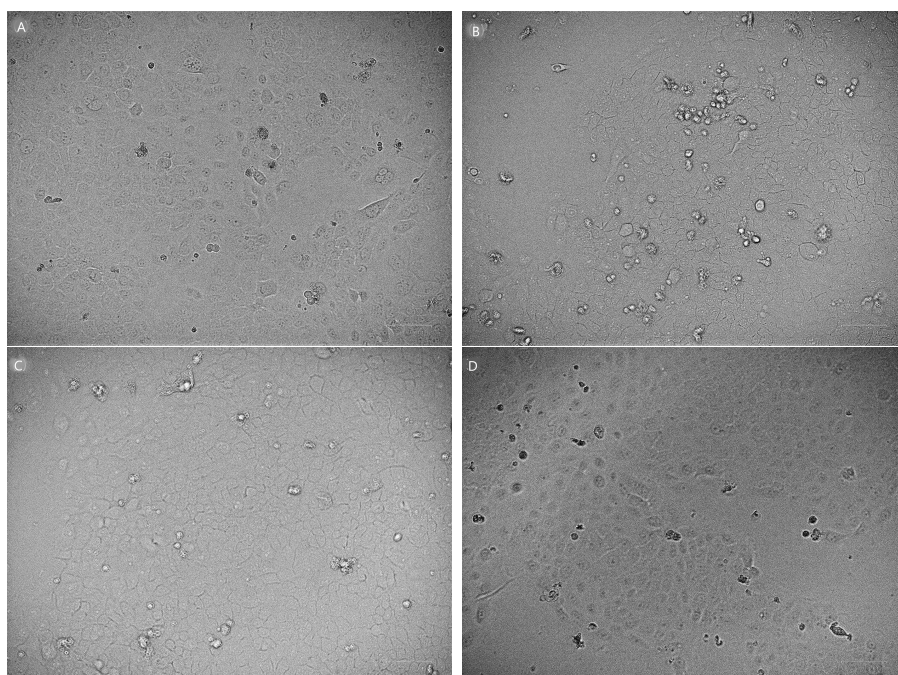


Figure 3.18: Cells treated with (a) 5 $\mu\text{g/mL}$, (b) 10 $\mu\text{g/mL}$, (c) 25 $\mu\text{g/mL}$ and (d) 50 $\mu\text{g/mL}$ of ZnO-PU NPs after 48 hours

3.2.6 Fluorescence Activated Cell Sorter (FACS)

FACS analysis results showed a low percentage of cell internalization both for ZnO NPs (about 2,1 %) and ZnO-PU NPs (about 1,1 %). From the graphs reported in Fig. 3.19 and data listed in Table 3.10, we can observe that the cell population in the fluorescence-positive quadrants increases when comparing to the control samples (untreated cells). Cell internalization is slightly higher for ZnO NPs, this may indicate that the polymer coating may reduce the intensity of the fluorochrome attached to ZnO NPs.

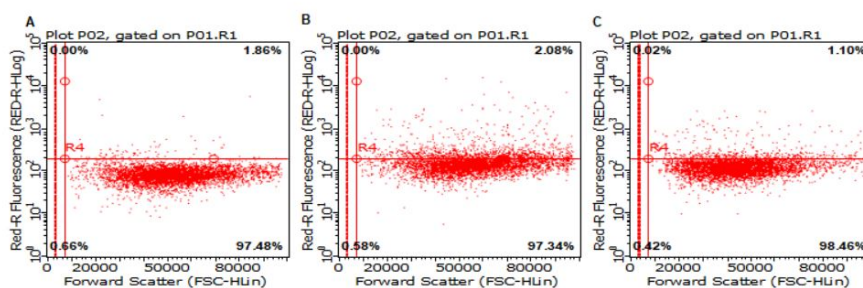


Figure 3.19: FACS analysis outcomes for (A) untreated cells (control) and cells treated with (B) ZnO NPs and (C) ZnO-PU NPs

Sample	Average Value
Control Sample	82,3
ZnO NPs	146,1
ZnO-PU NPs	123,4

Table 3.10: FACS average values

Chapter 4

Conclusions

PDAC is one of the most lethal solid tumours because of its difficult diagnosis [4]. This is mainly due to the heterogeneity of PDAC microenvironment which impedes the accumulation of drugs in tumor site. For this reason, new approaches based on nanomedicine were developed to overcome the limitations of the traditional treatments, such as chemotherapy or radiotherapy. Nanomedicine gives new tools more specific and selective to treat PDAC. We decided to focus on ZnO nanoparticles and Gd-doped ones by virtue of their characteristic properties, including reduced size, low cytotoxicity and antimicrobial properties [32]. In addition, we decided to coat these nanoparticles with a polymer and stabilize them with a lipid bilayer to enhance their biocompatibility.

Results showed that the synthesized inorganic nanoparticles had a small size, which increased with the presence of the coating, useful for cellular encapsulation. After coating, the surface charge of ZnO and ZnOGd nanoparticles switched from positive to negative values, demonstrating the effective coating of the inorganic core with the polyurethane shell. Viability test performed on NPs showed that the percentage of viable cells increased when reducing the concentration of nanoparticles, both for uncoated and coated ZnO and ZnOGd nanoparticles. Comparing coated and uncoated nanoparticles, the number of viable cells increased with the presence of the polymer coating, demonstrating its ability to improve the biocompatibility of the inorganic NPs.

The system showed some useful features for PDAC treatment. Firstly, the nanoparticles size was small enough (in the typical range of 5-100 nm) to allow cell internalization. Moreover, the positive charge of ZnO and ZnOGd NPs, enhanced with the amine-functionalization, improved the conjugation with the polymer which had a negative charge, allowing the formation of a polymer shell surrounding the inorganic core. TEM images confirmed this assertion, showing that for an initial inorganic core loading of 20 μg , effective encapsulation and little aggregation was achieved. Encapsulation was also confirmed by the quantification of ZnO

loaded inside the coating. The efficacy of encapsulation of ZnO inside the coated nanostructure was over the 50 %.

Viability test showed that concentrations of bare ZnO and ZnO-Gd nanoparticles over 10 $\mu\text{g}/\text{mL}$ resulted in higher toxicity against BxPC-3 cells, which was significantly decreased with the coated nanoparticles. Therefore, the polymer coating seems to impart higher biocompatibility to the system.. As demonstrated from these results, this system could represent a potential nanomedicine tool to treat pancreatic cancer by virtue of its high loading, reduced toxicity, and combination of imaging capacity given by the inorganic core. This work aimed at the synthesis of the nanoparticles and their primary characterizations to evaluate the possibility of use them in PDAC treatment. Overall, our results demonstrate that ZnO and ZnOGd NPs can be coated with a polymer shell with high loading efficiency and that coating results in enhanced biocompatibility. These results are promising and should be further expanded. For instance, the shell of the NPs can be exploited for ligand coupling to achieve a more selective cancer treatment. Nanoparticles could be loaded with different drugs and tested on different types of pancreatic cancer cells and on different culture conditions (e.g., in 3D spheroid models). Another aspect which could be analyzed more in details is the improvement of the imaging capacity for magnetic resonance imaging.

Bibliography

- [1] Giulia Brachi, Federico Bussolino, Gianluca Ciardelli, and Clara Mattu. «Nanomedicine for imaging and therapy of pancreatic adenocarcinoma». In: *Frontiers in bioengineering and biotechnology* 7 (2019), p. 307 (cit. on pp. 1, 2, 9, 11).
- [2] Guihua Jin, Weilong Hong, Yangyang Guo, Yongheng Bai, and Bicheng Chen. «Molecular mechanism of pancreatic stellate cells activation in chronic pancreatitis and pancreatic cancer». In: *Journal of Cancer* 11.6 (2020), p. 1505 (cit. on p. 1).
- [3] Stephanie K Dougan. «The pancreatic cancer microenvironment». In: *The Cancer Journal* 23.6 (2017), pp. 321–325 (cit. on pp. 1, 2).
- [4] Won Jin Ho, Elizabeth M Jaffee, and Lei Zheng. «The tumour microenvironment in pancreatic cancer—clinical challenges and opportunities». In: *Nature Reviews Clinical Oncology* 17.9 (2020), pp. 527–540 (cit. on pp. 2, 3, 52).
- [5] Aleksandra Adamska, Alice Domenichini, and Marco Falasca. «Pancreatic ductal adenocarcinoma: current and evolving therapies». In: *International journal of molecular sciences* 18.7 (2017), p. 1338 (cit. on pp. 1, 5–8).
- [6] Robert W Cowan and Anirban Maitra. «Genetic progression of pancreatic cancer». In: *The Cancer Journal* 20.1 (2014), pp. 80–84 (cit. on pp. 3, 4).
- [7] Ralph H Hruban, Anirban Maitra, and Michael Goggins. «Update on pancreatic intraepithelial neoplasia». In: *International journal of clinical and experimental pathology* 1.4 (2008), p. 306 (cit. on pp. 3, 4).
- [8] B Sipos, S Frank, T Gress, S Hahn, and G Klöppel. «Pancreatic intraepithelial neoplasia revisited and updated». In: *Pancreatology* 9.1-2 (2009), pp. 45–54 (cit. on pp. 3, 4).
- [9] Sally A El-Zahaby, Yosra SR Elnaggar, and Ossama Y Abdallah. «Reviewing two decades of nanomedicine implementations in targeted treatment and diagnosis of pancreatic cancer: An emphasis on state of art». In: *Journal of Controlled Release* 293 (2019), pp. 21–35 (cit. on pp. 5, 9).

- [10] Stephanie Tran, Peter-Joseph DeGiovanni, Brandon Piel, and Prakash Rai. «Cancer nanomedicine: a review of recent success in drug delivery». In: *Clinical and translational medicine* 6.1 (2017), pp. 1–21 (cit. on p. 8).
- [11] Marco Carofiglio, Sugata Barui, Valentina Cauda, and Marco Laurenti. «Doped zinc oxide nanoparticles: Synthesis, characterization and potential use in nanomedicine». In: *Applied Sciences* 10.15 (2020), p. 5194 (cit. on pp. 8, 9, 12, 13, 16).
- [12] Chitta Ranjan Patra et al. «Targeted delivery of gemcitabine to pancreatic adenocarcinoma using cetuximab as a targeting agent». In: *Cancer research* 68.6 (2008), pp. 1970–1978 (cit. on p. 9).
- [13] Sara Trabulo, Antonio Aires, Alexandra Aicher, Christopher Heeschen, and Aitziber L Cortajarena. «Multifunctionalized iron oxide nanoparticles for selective targeting of pancreatic cancer cells». In: *Biochimica et Biophysica Acta (BBA)-General Subjects* 1861.6 (2017), pp. 1597–1605 (cit. on p. 9).
- [14] Christopher C DuFort et al. «Interstitial pressure in pancreatic ductal adenocarcinoma is dominated by a gel-fluid phase». In: *Biophysical journal* 110.9 (2016), pp. 2106–2119 (cit. on p. 9).
- [15] Jun-Tao Dai, Yu Zhang, Heng-Chao Li, Yong-Hui Deng, Ahmed A Elzatahry, Abdulaziz Alghamdi, De-Liang Fu, Yong-Jian Jiang, and Dong-Yuan Zhao. «Enhancement of gemcitabine against pancreatic cancer by loading in mesoporous silica vesicles». In: *Chinese Chemical Letters* 28.3 (2017), pp. 531–536 (cit. on p. 9).
- [16] FM Martín-Saavedra, E Ruiz-Hernández, A Boré, D Arcos, M Vallet-Regí, and N Vilaboa. «Magnetic mesoporous silica spheres for hyperthermia therapy». In: *Acta Biomaterialia* 6.12 (2010), pp. 4522–4531 (cit. on p. 10).
- [17] F Joubert and G Pasparakis. «Hierarchically designed hybrid nanoparticles for combinational photochemotherapy against a pancreatic cancer cell line». In: *Journal of Materials Chemistry B* 6.7 (2018), pp. 1095–1104 (cit. on p. 10).
- [18] Sivasai Balivada et al. «A/C magnetic hyperthermia of melanoma mediated by iron (0)/iron oxide core/shell magnetic nanoparticles: a mouse study». In: *BMC cancer* 10.1 (2010), pp. 1–9 (cit. on p. 10).
- [19] Melissa S Wason, Heng Lu, Lin Yu, Satadru K Lahiri, Debarati Mukherjee, Chao Shen, Soumen Das, Sudipta Seal, and Jihe Zhao. «Cerium oxide nanoparticles sensitize pancreatic cancer to radiation therapy through oxidative activation of the JNK apoptotic pathway». In: *Cancers* 10.9 (2018), p. 303 (cit. on p. 10).

- [20] Cailian Wang, Haijun Zhang, Baoan Chen, Haitao Yin, and Wenwen Wang. «Study of the enhanced anticancer efficacy of gambogic acid on Capan-1 pancreatic cancer cells when mediated via magnetic Fe₃O₄ nanoparticles». In: *International journal of nanomedicine* 6 (2011), p. 1929 (cit. on p. 10).
- [21] Preeti Nigam Joshi, Sachin Agawane, Meghana C Athalye, Vrushali Jadhav, Dhiman Sarkar, and Rajiv Prakash. «Multifunctional inulin tethered silver-graphene quantum dots nanotheranostic module for pancreatic cancer therapy». In: *Materials Science and Engineering: C* 78 (2017), pp. 1203–1211 (cit. on pp. 10, 11).
- [22] Krishnendu Pal, Farah Al-Suraih, Roberto Gonzalez-Rodriguez, Shamit Kumar Dutta, Enfeng Wang, H Shaun Kwak, Thomas R Caulfield, Jeffery L Coffey, and Santanu Bhattacharya. «Multifaceted peptide assisted one-pot synthesis of gold nanoparticles for plectin-1 targeted gemcitabine delivery in pancreatic cancer». In: *Nanoscale* 9.40 (2017), pp. 15622–15634 (cit. on p. 11).
- [23] Feng Yin et al. «SiRNA delivery with PEGylated graphene oxide nanosheets for combined photothermal and genetherapy for pancreatic cancer». In: *Theranostics* 7.5 (2017), p. 1133 (cit. on p. 11).
- [24] Paul Cherukuri, Evan S Glazer, and Steven A Curley. «Targeted hyperthermia using metal nanoparticles». In: *Advanced drug delivery reviews* 62.3 (2010), pp. 339–345 (cit. on pp. 11, 12).
- [25] Adeolu Oluwasanmi, Wejdan Al-Shakarchi, Ayesha Manzur, Mohammed H Aldebasi, Rayan S Elsini, Malek K Albusair, Katherine J Haxton, Anthony DM Curtis, and Clare Hoskins. «Diels Alder-mediated release of gemcitabine from hybrid nanoparticles for enhanced pancreatic cancer therapy». In: *Journal of Controlled Release* 266 (2017), pp. 355–364 (cit. on p. 11).
- [26] Priyanka Ray, Narendra Kale, and Mohiuddin Quadir. «New side chain design for pH-responsive block copolymers for drug delivery». In: *Colloids and Surfaces B: Biointerfaces* 200 (2021), p. 111563 (cit. on p. 11).
- [27] B Dumontel, M Canta, H Engelke, A Chiodoni, L Racca, A Ancona, T Limongi, G Canavese, and V Cauda. «Enhanced biostability and cellular uptake of zinc oxide nanocrystals shielded with a phospholipid bilayer». In: *Journal of Materials Chemistry B* 5.44 (2017), pp. 8799–8813 (cit. on pp. 12, 13, 18, 36).
- [28] John W Rasmussen, Ezequiel Martinez, Panagiota Louka, and Denise G Wingett. «Zinc oxide nanoparticles for selective destruction of tumor cells and potential for drug delivery applications». In: *Expert opinion on drug delivery* 7.9 (2010), pp. 1063–1077 (cit. on pp. 12, 14).

- [29] Sugata Barui, Roberto Gerbaldo, Nadia Garino, Rosaria Brescia, Francesco Laviano, and Valentina Cauda. «Facile Chemical Synthesis of Doped ZnO Nanocrystals Exploiting Oleic Acid». In: *Nanomaterials* 10.6 (2020), p. 1150 (cit. on pp. 12, 13, 16, 17, 37, 38).
- [30] Marco Laurenti and Valentina Cauda. «ZnO nanostructures for tissue engineering applications». In: *Nanomaterials* 7.11 (2017), p. 374 (cit. on p. 12).
- [31] P Maddahi, N Shahtahmasebi, Ahmad Kompany, Mansour Mashreghi, Samira Safaee, and Fateme Roozban. «Effect of doping on structural and optical properties of ZnO nanoparticles: study of antibacterial properties». In: *Materials Science-Poland* 32.2 (2014), pp. 130–135 (cit. on pp. 12, 13).
- [32] Gunjan Bisht and Sagar Rayamajhi. «ZnO nanoparticles: a promising anti-cancer agent». In: *Nanobiomedicine* 3.Godište 2016 (2016), pp. 3–9 (cit. on pp. 12, 13, 52).
- [33] Marco Carofiglio, Marco Laurenti, Veronica Vighetto, Luisa Racca, Sugata Barui, Nadia Garino, Roberto Gerbaldo, Francesco Laviano, and Valentina Cauda. «Iron-Doped ZnO Nanoparticles as Multifunctional Nanoplatfoms for Theranostics». In: *Nanomaterials* 11.10 (2021), p. 2628 (cit. on p. 13).
- [34] C Mattu et al. «Alternating block copolymer-based nanoparticles as tools to modulate the loading of multiple chemotherapeutics and imaging probes». In: *Acta biomaterialia* 80 (2018), pp. 341–351 (cit. on p. 13).
- [35] Carmen Iodice et al. «Enhancing photothermal cancer therapy by clustering gold nanoparticles into spherical polymeric nanoconstructs». In: *Optics and Lasers in Engineering* 76 (2016), pp. 74–81 (cit. on p. 13).
- [36] Renliang Xu. «Progress in nanoparticles characterization: Sizing and zeta potential measurement». In: *Particuology* 6.2 (2008), pp. 112–115 (cit. on p. 19).
- [37] Sourav Bhattacharjee. «DLS and zeta potential—what they are and what they are not?». In: *Journal of controlled release* 235 (2016), pp. 337–351 (cit. on pp. 19, 20).
- [38] J Epp. «X-ray diffraction (XRD) techniques for materials characterization». In: *Materials characterization using nondestructive evaluation (NDE) methods*. Elsevier, 2016, pp. 81–124 (cit. on pp. 21, 22).
- [39] Ashish Chauhan and Priyanka Chauhan. «Powder XRD technique and its applications in science and technology». In: *J Anal Bioanal Tech* 5.5 (2014), pp. 1–5 (cit. on p. 21).
- [40] Martin Ermrich and Detlef Opper. «XRD for the analyst». In: *Getting acquainted with the principles. Second. Panalytical* (2013) (cit. on p. 22).

- [41] D Rajesh, B Vara Lakshmi, and CS Sunandana. «Two-step synthesis and characterization of ZnO nanoparticles». In: *Physica B: Condensed Matter* 407.23 (2012), pp. 4537–4539 (cit. on p. 23).
- [42] D Semnani. «Geometrical characterization of electrospun nanofibers». In: *Electrospun Nanofibers*. Elsevier, 2017, pp. 151–180 (cit. on p. 24).
- [43] Soham Shukla. «Freeze drying process: A review». In: *International journal of pharmaceutical sciences and research* 2.12 (2011), p. 3061 (cit. on p. 26).
- [44] Kunal A Gaidhani, Mallinath Harwalkar, Deepak Bhambere, and Pallavi S Nirgude. «Lyophilization/freeze drying—a review». In: *World journal of pharmaceutical research* 4.8 (2015), pp. 516–543 (cit. on pp. 26, 27).
- [45] CY Tang and Z Yang. «Transmission electron microscopy (TEM)». In: *Membrane Characterization*. Elsevier, 2017, pp. 145–159 (cit. on p. 28).
- [46] Deena Titus, E James Jebaseelan Samuel, and Selvaraj Mohana Roopan. «Nanoparticle characterization techniques». In: *Green synthesis, characterization and applications of nanoparticles*. Elsevier, 2019, pp. 303–319 (cit. on p. 28).
- [47] James W Tung, David R Parks, Wayne A Moore, Leonard A Herzenberg, and Leonore A Herzenberg. «New approaches to fluorescence compensation and visualization of FACS data». In: *Clinical immunology* 110.3 (2004), pp. 277–283 (cit. on p. 30).
- [48] Surabhi Siva Kumar, Putcha Venkateswarlu, Vanka Ranga Rao, and Gollapalli Nageswara Rao. «Synthesis, characterization and optical properties of zinc oxide nanoparticles». In: *International Nano Letters* 3.1 (2013), pp. 1–6 (cit. on p. 37).
- [49] P Vanathi, P Rajiv, S Narendhran, Sivaraj Rajeshwari, Pattanathu KSM Rahman, and Rajendran Venckatesh. «Biosynthesis and characterization of phyto mediated zinc oxide nanoparticles: a green chemistry approach». In: *Materials Letters* 134 (2014), pp. 13–15 (cit. on p. 45).